JGR Atmospheres

RESEARCH ARTICLE
10.1029/2023JD039493

The Role of the Toroidal Vortex in Cumulus Clouds' Entrainment and Mixing

Eshkol Eytan[1,2], Yael Arieli[1], Alexander Khain[3], Orit Altaratz[1], Mark Pinsky[3†], Ehud Gavze[3], and Ilan Koren[1]

[1]Department of Earth and Planetary Science, Weizmann Institute of Science, Rehovot, Israel, [2]Now at the Cooperative Institute for Research in Environmental Sciences, University of Colorado and NOAA Chemical Science Laboratory, Boulder, CO, USA, [3]Institute of Earth Science, Hebrew University, Jerusalem, Israel

†Deceased 24 February 2024

Key Points:

- Coherent and turbulent toroidal (ring) vortices are presented in 10 m resolution LES of shallow cumulus clouds
- The toroidal vortex dominates the cloud's dilution, as shown by the cloud's lateral mass flux profile and Eulerian tracers analysis
- Lagrangian tracers reveal that most entrained air is environmental (not recycled by the vortex) with high relative humidity

Supporting Information:

Supporting Information may be found in the online version of this article.

Correspondence to:

I. Koren,
Ilan.Koren@weizmann.ac.il

Citation:

Eytan, E., Arieli, Y., Khain, A., Altaratz, O., Pinsky, M., Gavze, E., & Koren, I. (2024). The role of the toroidal vortex in cumulus clouds' entrainment and mixing. *Journal of Geophysical Research: Atmospheres*, *129*, e2023JD039493. https://doi.org/10.1029/2023JD039493

Received 5 JUL 2023
Accepted 18 JUN 2024

Author Contributions:

Conceptualization: Eshkol Eytan, Alexander Khain, Ilan Koren
Data curation: Eshkol Eytan
Formal analysis: Eshkol Eytan
Investigation: Eshkol Eytan
Methodology: Eshkol Eytan, Alexander Khain, Orit Altaratz, Ilan Koren
Software: Eshkol Eytan, Yael Arieli
Supervision: Alexander Khain, Ilan Koren
Writing – original draft: Eshkol Eytan, Yael Arieli, Alexander Khain, Orit Altaratz, Mark Pinsky, Ehud Gavze, Ilan Koren

Abstract Shallow convective clouds play a crucial role in Earth's energy budget, as they modulate the radiative transfer in the atmosphere and participate in the vertical transport of aerosols, energy, and humidity. The parameterizations representing these complex, vital players in weather and climate models are mostly based on a description of steady-state plumes and are a source of major uncertainty. Recently, several studies have shown that buoyant thermals are inherent in atmospheric convection and contain a toroidal (ring) vortex. This work studies those vortices in growing shallow cumulus (Cu) clouds using high-resolution (10 m) Large Eddy Simulations that resolve these vortices in much detail. Recent analysis of such data showed that small-scale turbulent diffusion is unable to explain the large diluted portion of the cloud. Here we advocate for the important role of the Cu toroidal vortex (TV) in cloud dilution and present the complex dynamics and structure of a Cu TV. Nevertheless, since the vortex dominates the cloud's dilution, simplicity emerges when considering the cloud's lateral mass flux profile. The cloud mixing is quantified using direct flux calculations and Eulerian tracers. In addition, Lagrangian tracers are used to identify the origin of the entrained air and its thermodynamic properties. It shows that most of the air entrained by the vortex is not recycled by the vortex, yet is significantly more humid than the environment. We suggest that the development of new models describing thermals, together with their toroidal vortices, might improve cloud parameterizations in weather and climate models.

Plain Language Summary Shallow convective clouds play a crucial role in climate as they transfer heat in the vertical dimension and affect radiation transfer in the atmosphere. These clouds are much smaller than climate models' resolution, and so they are represented by simplified equations in weather and climate models (parameterizations). This simple representation of such important processes is one of the largest sources of uncertainty in climate models. In particular, the process of clouds mixing with their dry surroundings is known to have a large contribution to the uncertainty reflected by clouds in climate prediction. In this work, we use high-resolution simulations of cumulus clouds to investigate the toroidal (ring) vortex that is located at the top of a rising thermal (a known property of cumulus dynamics). We show that cloud-scale vortices dominate cloud dilution and are at least as important as stochastic turbulent motions which are often considered in mixing parameterizations. These ideas can serve for future parameterizations of shallow cumulus clouds in coarse-resolution models.

1. Introduction

Clouds play an enormous role in Earth's energy budget, as their hydrometeors interact strongly with both solar and terrestrial radiation (Allan, 2011; Trenberth et al., 2009). Cumulus clouds (Cu) also participate in the vertical transport of mass from the boundary layer into the free atmosphere, redistributing gas tracers, aerosols, humidity, heat, and momentum. Shallow Cu clouds act to precondition the atmosphere for deeper clouds' formation via this transport (see Champouillon et al. (2023) and references therein). Inaccurate representation of shallow Cu clouds was shown to cause errors in the modeling of deep convective systems, such as those related to the Madden-Julian Oscillation and in the diurnal timing of the transition from shallow to deep convection over land (Rio et al., 2019; Savarin & Chen, 2022). Shallow Cu clouds cannot be directly resolved in large-scale models (i.e., weather and climate) due to their small size compared to the grid scale and are hence parameterized. Parameterizing such complex and important players in Earth's energy budget induce high model sensitivity to the chosen parametrization scheme (and its parameters) and to large uncertainty in climate prediction (Klocke et al., 2011; Rio

et al., 2019; Romps, 2016; Rougier et al., 2009; Tsushima et al., 2020; Villalba-Pradas & Tapiador, 2022; Zelinka et al., 2020).

How Cu clouds mix with their environment and the mixing effects on clouds' microphysical, dynamical, and morphological properties are burning questions in cloud physics (De Rooy et al., 2013; Heus et al., 2008; Khain & Pinsky, 2018; Lim & Hoffmann, 2023). Convection is usually represented by transient bubble or steady-state plume models (Romps et al., 2021). Yano (2014) presents an extensive overview of this discussion that goes back to the 1950s. Most large-scale models today use the eddy diffusivity-mass flux parameterization (Arakawa & Schubert, 1974; Kain & Fritsch, 1990; Tiedtke, 1989), which treats clouds as buoyant, steady-state, horizontally homogeneous plumes that entrain environmental air from the sides by turbulent motion (De Rooy et al., 2013). This is in contrast to numerous studies showing that Cu clouds consist of thermals (French et al., 1999; Hernandez-Deckers et al., 2022; Heus et al., 2009; Romps et al., 2021; Zhao & Austin, 2005b), which are transient parcels with a short lifetime of several minutes (Romps & Charn, 2015; Sherwood et al., 2013). Such thermals will probably be better represented by a bubble model. Turner (1962) suggested a hybrid model called the starting plume, representing a plume with a leading bubble cap. This concept, which has been mostly overlooked in Cu parameterizations so far (Yano, 2014), was recently examined by Pinsky et al. (2022, 2023) and shown to adequately represent liquid water content and vertical velocity of a growing shallow Cu inside a thermal and in its trailing wake or non-stationary jet.

The steady-state assumption can be justified by considering that the parametrization aims to represent a cloud ensemble (i.e., cloud field). However, assuming that clouds mix with pure (i.e., far) environmental air, leads to a significant bias in the diagnosed bulk entrainment rate (even by a factor of 2) due to the humid surroundings of the clouds (Romps, 2010). Another substantial deficiency in the convective parametrizations is the assumption of horizontal homogeneity in the plume models. The interaction of thermals with other parts of the cloud and the environment produces horizontal gradients and variability in cloud properties (as demonstrated by high-frequency in situ observations, Gerber, 2000; Gerber et al., 2008; Konwar et al., 2021) down to a scale of tens of centimeters (Lehmann et al., 2009). The horizontal gradients spread outside the cloud, forming a humid subsiding shell around it (Heus & Jonker, 2008; Laird, 2005; Perry & Hobbs, 1996). Eytan et al. (2022) simulated single shallow cumulus clouds in high-resolution of 10 m with a detailed representation of the microphysical process (spectral bin scheme; Khain et al., 2004). They performed accurate quantification of the dilution state of different parts in the clouds (according to Eytan et al. (2021)) and identified small undiluted volumes near the cloud top. These undiluted core fragments correspond to the idea of convective thermals and support the concept of bubbles. The abovementioned findings are in agreement with the results and view suggested recently by Hernandez-Deckers et al. (2022), who stated that thermals are the building blocks of convection.

Eytan et al. (2022) also demonstrated the existence of a narrow transition zone at the cloud edge (on a scale of tens of meters) with sharp gradients in cloud microphysical properties. This zone, whose presence is further corroborated by high-frequency in situ measurements (Gerber, 2000; Katzwinkel et al., 2014) and a theoretical diffusion-evaporation toy model (Pinsky & Khain, 2018), suggests that turbulent diffusion by mixing can explain only the intense dilution that occurs up to several tens of meters away from the edges and into the cloud. Arieli et al. (2024) had recently used Lagrangian tracers to show how the cloud can be separated into three distinct regimes: transition zone (cloud's skin), core, and periphery. This raises the question of what process generates diluted volumes deep in the cloud. Pinsky et al. (2021) applied wavelet filtering to the same data set as (Eytan et al., 2022) and developed a novel method separating the convective (cloud scale) and turbulent (smaller scale) motions. They showed that many cloud properties could be explained by non-turbulent motions on the scale of tens to hundreds of meters that can be represented using equations of advection (Pinsky et al., 2022).

A persistent feature of rising thermals is the toroidal vortex (TV) (i.e., ring vortex; Meleshko et al. (2012)), which was documented in convective clouds by observations (Damiani et al., 2006; Wang & Geerts, 2015) and modeling (Romps & Charn, 2015; Sherwood et al., 2013; Strauss et al., 2022; Zhao & Austin, 2005b). The TV was suggested to play an important role in Cu dynamics and life cycle by greatly contributing to clouds' mixing with their environment (Carpenter et al., 1998; Morrison et al., 2022; Vybhav & Ravichandran, 2022; Yano, 2014; Zhao & Austin, 2005b). Recently, it was also suggested that the TV affects the microphysical cloud structure and biases adiabatic fraction (AF) estimations near the cloud top and away from the undiluted core (Eytan et al., 2021). There are some established analytical solutions to describe the TV (Hill, 1894; Meleshko et al., 2012), including a theory for Cu (Levine, 1959). Recent studies advanced the understanding of a thermal TV (driven by buoyancy) and

developed models to describe it (McKim et al., 2020; Morrison et al., 2021, 2022; Vybhav & Ravichandran, 2022; Yano, 2023). A TV located near the upper part of an ascending cloud should detrain air at the cloud top and re-entrain it from the cloud's sides at lower altitudes. Such a flow pattern can potentially bridge the gap between the cloud-top versus lateral mixing theories (Heus et al., 2008) and explain some observations suggesting cloud-top mixing (e.g., Paluch, 1979). We note that most of the studies of thermals and their accompanied toroidal vortices either use simulation with relatively coarse resolution of 50–100 m that doesn't resolve some of the fine details in space and time or are based on simplified toy models. All of the above suggest that thermals and their TV are good candidates to be the bases of new parametrization schemes that might be more adequate at representing convective clouds in large-scale models; such efforts have been recently made by Morrison et al. (2020) and Pinsky et al. (2023).

This study uses high-resolution (10 m) simulations of single shallow Cu clouds with passive tracers to define the structure and evolution of the TV and investigate its role in diluting and mixing the clouds with their environment. The study is motivated to explain the appearance of large volumes of diluted air in a Cu cloud that cannot be explained by small-scale turbulent diffusion and to paint a more vivid picture of the TV that appears in convective moist thermals. How and on what scale can one define these vortices, what is their life cycle, how coherent they are, and do they recirculate air at the top of an ascending Cu? The structure of the paper is as follows: Section 2 provides the simulation details and analysis methodology; Section 3 presents the methods used to define the TV and its unique properties in Cu; Section 4 reveals the relationship of the TV to cloud dynamics and its effects on the cloud surroundings, quantifies the contribution of the TV to mixing, and presents its effects on the internal cloud structure; In Section 5, we discuss the potential of a well-established theory for thermals and their TV to improve Cu parametrizations in weather and climate models.

2. Materials and Methods

2.1. Model Description and Simulation Design

The trade Cu clouds were simulated using the System of Atmospheric Modeling (SAM, Khairoutdinov & Randall, 2003) with a grid spacing of 10 m and a time step of 0.5s. The sub-grid turbulence parameterization was a 1.5-closure scheme, as presented in Khairoutdinov and Kogan (1999). The model was coupled to a Spectral Bin Microphysical scheme (SBM, Fan et al., 2009; Khain et al., 2004). The simulations were initialized using the BOMEX case study setup, including the vertical profiles of the water vapor mixing ratio and potential temperature with inversion at 1,500–2,000 m (Siebesma et al., 2003). The horizontal background wind was set to zero. The convective motion was initialized by an instantaneous thermal perturbation shaped as a cylinder with a 500 m radius and 100 m depth (from the surface). The perturbation magnitude decayed from the center toward the edge as a cosine squared function, and random noise was superimposed on the perturbation to initiate turbulence. More details of the simulations can be found in Eytan et al. (2021). Three different simulations were used in this study: The first simulated cloud (upper row in Figure 1) was initiated with a temperature perturbation of 0.1 K at the center. This cloud developed with one dominant updraft pulse (as will be shown in Sections 3 and 4). The second simulated cloud (bottom row of Figure 1) was initiated with a weaker thermal perturbation of 0.01 K. Accordingly, it appeared later but developed to be larger and lived longer. This cloud developed as multiple updraft pulses (a succession of thermals). The third simulation was similar to the first one except for the random noise and output frequency (2 compared to 30 s). This simulation was used for the Lagrangian particle analysis described below.

2.2. Eulerian Tracers

For quantifying the dilution level in different regions of the cloud, we added two conservative scalars (passive tracers) to the simulations as part of the initialization process. These tracers disperse in space and time by advection and turbulent diffusion according to the sub-grid schemes. The first tracer was uniformly distributed in the sub-cloud layer, from the surface up to 600 m (mean cloud base height). This tracer, which penetrated the cloud through its base, provided an accurate measure for dilution. Throughout the paper, the tracers' mixing ratio was normalized by the sub-cloud initial mixing ratio value. This normalized variable is referred to as cTr, such that $cTr = 1$ indicates no dilution. Note that the absolute value of the tracer's mixing ratio is insignificant as it doesn't affect the dynamics, and is always normalized by its initial value. A second tracer is an environmental tracer (eTr), which was distributed initially in the cloudy and inversion layers between 600 and 2,000 m.

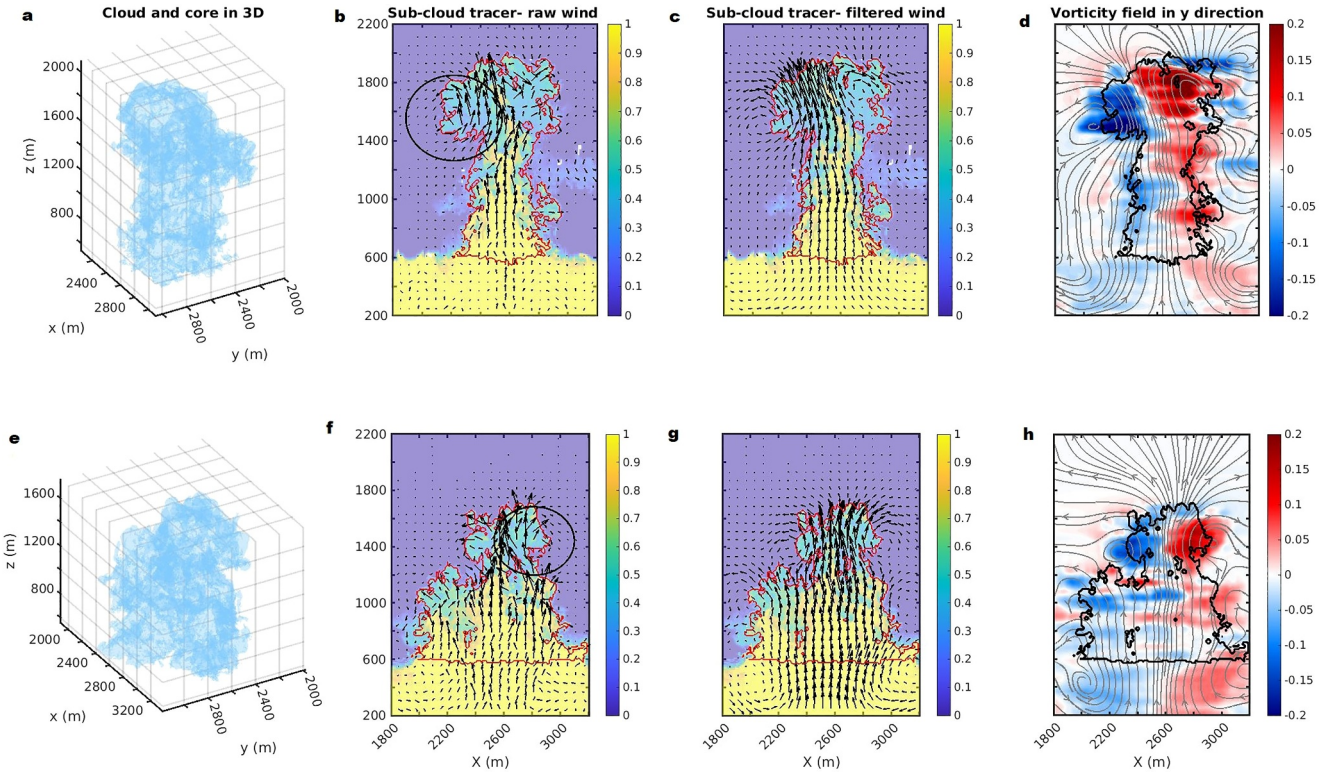

Figure 1. *Snapshots of two simulated clouds visualizing the toroidal vortex* (TV). *First row*—a single-bubble cloud in its mature stage: (a) A 3D visualization of the cloud's envelope. (b) A vertical cross-section of the sub-cloud tracer (cTr); the cloud edge is marked by a red contour ($q_l = 0.01$ gkg^{-1}) and velocity arrows are in black. A black circle marks the flow pattern of the TV. (c) Same as (b) but with a 3D filtered velocity field revealing the signature of the TV. The filter was a moving average at a size of $410 \times 410 \times 50$ m in the x, y, and z directions, respectively. (d) A vorticity field in the y direction with streamlines presenting the flow. Black contour is the cloud edge. *Second row*—the same as the first row but for a cloud comprised of several bubbles during its growth stage (panels (e–h) correspond to (a–d), respectively).

Comparing the density values of the two tracers revealed that their mixing can be approximated as linear, such that $cTr \approx 1 - eTr$. Eytan et al. (2021) used such passive tracers to validate different AF calculation methods. $AF = \frac{LWC}{LWC_{ad}}$, where LWC is the liquid water content in gkg^{-1}, and $LWC_{ad}(z)$ is the amount of liquid water a parcel would have if it was lifted adiabatically to an altitude z. In a non-precipitating cloud most of the deviation of LWC from LWC_{ad} would result from mixing with the environment. They found that one method was better than others and yielded a good agreement between the values of AF and cTr deep in the clouds (away from the cloud edge, where evaporation acts as an additional sink for AF). Using the optimal method from that study, we found that away from the cloud edge, the difference between $(1 - eTr)$ and AF was negligible, with a mean of 0.02 and a standard deviation of 0.08; the median difference was 10^{-5}. Hence, in this work, for the sake of comparing the fictitious tracers with the "real" and measurable AF, one can assume that $AF \approx cTr \approx 1 - eTr$. AF was shown to determine the clouds' microphysical parameters (Eytan et al., 2022).

2.3. Lagrangian Tracers

An additional analysis performed in this work followed the trajectories of specific particles during the simulation (Lagrangian tracers). Their trajectories were calculated off-line using the 3D wind velocity field according to $X^i = X_0^i + U_0^i \Delta t$; where X^i is the coordinate in the ith direction, subscript 0 denotes the initial coordinate and velocity, and Δt is the time interval according to the model output rate (2 s in our case). The Lagrangian tracking was also carried out using an improved Euler scheme (Süli & Mayers, 2003) that included the particle's acceleration using a sub-step that predicts temporal position and velocity (i.e., a second-order scheme). The difference between the results produced by the two schemes is negligible, meaning that the chosen sampling frequency of 2 s is high compared to the numerical time step (0.5 s) and the physical timescales, allowing the use of a first-order Euler scheme. The velocity and other thermodynamic variables were linearly interpolated in 3D at the sub-grid position. $\sim 1.1 \cdot 10^6$ particles were released with a 10 m spacing in a square of 800×800 m^2 located around the

cloud's center. The particles were distributed between the altitudes of 300–2,000 m at the beginning of the cloud's lifetime (24 min of simulation). The definition of a tracer particle's entrance (or exit) to (or from) the cloud on a discrete numerical grid demands a binary definition of the cloud and its edge (a threshold of liquid water mixing ratio of 0.01 gkg^{-1} was used in our case). Because there was some uncertainty regarding both the exact location of the cloud edge (i.e., sub-grid location) and the particle's position, the entrance or exit to the cloud was defined only when the distance to the cloud edge (DFCE; calculated as in Eytan et al. (2022)) was larger than the simulation resolution (10 m). For more details see Arieli et al. (2024).

2.4. Lateral Mass Flux Estimation

A main part of this study was dedicated to the quantification of the entrainment mixing caused by the TV. It was estimated by calculating the lateral mass flux (LMF) into and out of the cloud for each vertical level by taking the following steps:

1. Determination of the cloud boundaries. The cloudy pixels for each vertical level were defined as those with liquid water mixing ratio >0.01 gkg^{-1}. Next, by using object detection according to pixel connectivity, we removed small fragments not connected to the main cloud. Straight lines between the points delineated a polygon of the cloud boundaries.
2. Defining the air velocity at the cloud boundaries. Interpolating the horizontal velocity and air density along the flanks of the polygon (marking the cloud boundaries) according to the neighboring grid points. Subsequently, obtaining the normal of the velocity vector to the cloud boundaries and calculating the fluxes at each point as the product of the normal component of the velocity $\left(u_{(x,y)} \cdot \hat{n}\right)$ and the air density $(\rho_{(x,y)})$.
3. Summing the total flux per height level. Integrating the flux along the cloud edge length (l) to obtain the total LMF into and out of the cloud (LMF) as

$$LMF_{(z)} = \int \rho_{(x,y,z)} u_{(x,y,z)} \cdot \hat{n} dl; \quad \left(\frac{kg}{ms}\right) \tag{1}$$

Equation 1 is a direct local estimation of fluxes in and out of the cloud (i.e., entrainment/detrainment). Other estimations of such fluxes were conducted before using different methods (Dawe & Austin, 2011; Romps, 2010; Zhao & Austin, 2005b). Dawe and Austin (2011) presented a method that considers the velocity differences between the air and the changing cloud edge, using sub-grid interpolation. Taking this into consideration, we conducted a sensitivity test. Its results showed that the uncertainty in the definition of the cloud boundaries polygon was larger than the errors introduced by neglecting the movement of the cloud edge. Therefore, we neglected it in our calculations. The results in Section 4 show good agreement with the results of Zhao and Austin (2005b) that used the continuity equation (comparing Figure 7 in their paper to Figure 5 here). Moreover, Dawe and Austin (2011) showed that the importance of their method is reduced with increasing resolution (see Figures 8 and 10 in their paper). We note that the spatial and temporal resolutions in our simulations were higher than the Dawe and Austin (2011) study (10 compared to 25 m, and time steps of 0.5 vs. 1.5 s). The aim of using LMF in this study was to capture the general behavior of mixing and relate it to the TV rather than provide an accurate estimate of fluxes.

3. The Toroidal Vortex in Shallow Cumulus Clouds

Figures 1a and 1e presents a visualization of the first two clouds (setup description in Section 2.1). The first cloud (upper row) is composed of a single updraft pulse driven by a dominant bubble. The second cloud (bottom row) was initiated with a weaker thermal perturbation, which generated a wider cloud that lived longer and was composed of multiple convective pulses. The second column in Figure 1 presents an x-z cross-section of cTr values along the center of the domain. The red contour marks the clouds' boundaries (liquid water mixing ratio of $q_l = 0.01$ gkg^{-1}), and the wind components in the x and z directions (u and w, respectively) are marked by black arrows. The yellow regions in the clouds mark the undiluted parts. It can be seen that the core is wide near the cloud base. It meanders and narrows with height until breaking into small core fragments, which can be regarded as a manifestation of bubbles.

The mushroom-like shape of the cloud suggests the presence of a TV near its top. On one side of the cloud top, the TV is easily revealed by a circular flow pattern, marked with black circles in Figures 1b and 1f. If the TV were a

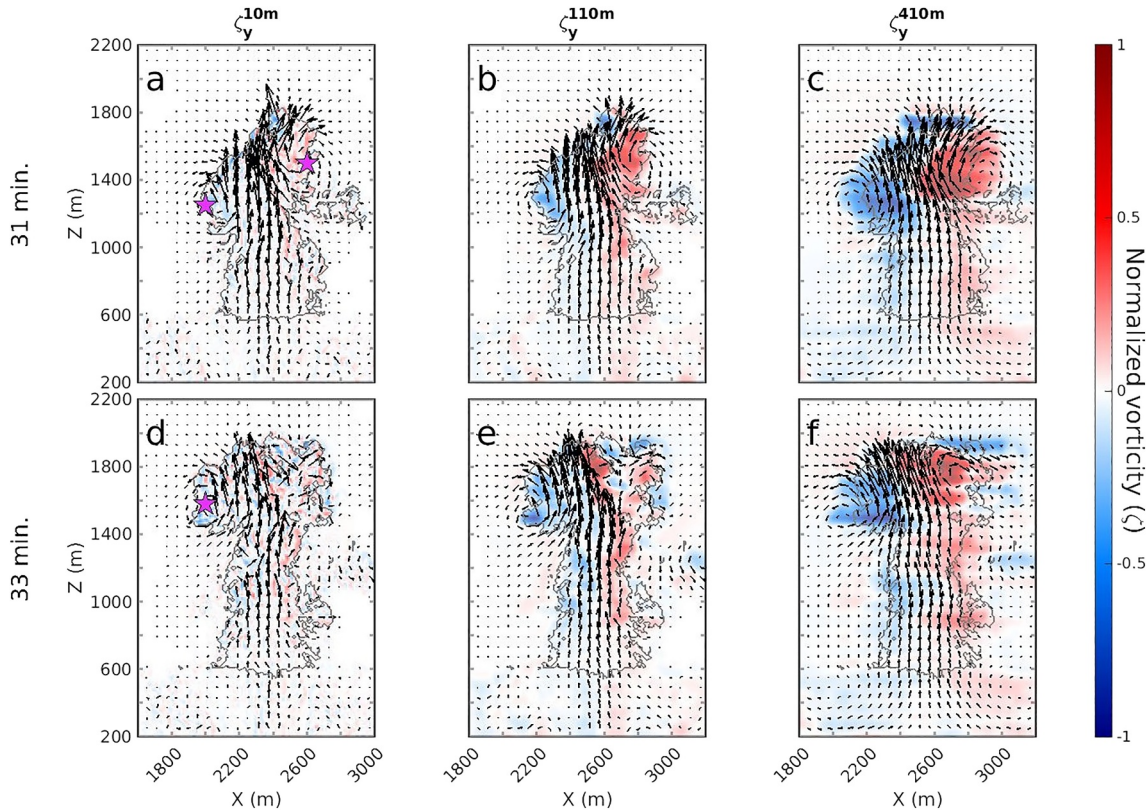

Figure 2. *The toroidal vortex* (TV) *at different times and averaging scales*. *x*-*z* cross sections of normalized vorticity (ζ) fields with the velocity filtered in different scales to show the dynamics of the vortex. Normalization was performed according to the maximal (minimal) value for all positive (negative) values, facilitating comparison between the cross-sections. ζ values decrease with filter size due to smoothing. Maximal ζ in absolute values are 6, 1, and 0.3 s^{-1} for the raw data, and filters 110 and 410 m, respectively. *First row*—The first cloud from Figure 1a during its growth stage at 31 min of simulation (11 min in the cloud's lifetime). The TV is clearly evident at all filtering scales. (a) Original resolution of 10 m. Magenta stars mark the center of the coherent vortex. (b) Filtered with a 110 × 110 × 50 m moving average. (c) Filtered with 410 × 410 × 50 m, as the third column of Figure 1. *Second row*—Same as the first row but for the cloud at 33 min of simulation, in its mature stage. The left side of the cloud shows a coherent vortex (marked by a magenta star), while on the right side, it appears only when filtered in the horizontal vortex scale.

perfect ring vortex, it would be axisymmetric around the cloud top, and its other side would have a similar counter-rotating vortex. This is not the case in Figure 1b, where a more complex pattern is observed. Filtering the flow field in the right scale (taken here as half of the horizontal scale of the cloud) removes the turbulent noise and extracts the "hidden" vortex. This is exhibited in Figure 1c, in which the flow was filtered by a moving averaging filter with a horizontal size of 410 m and a vertical size of 50 m. Figure 1d shows the filtered vorticity field overlaid with streamlines. The two fields clearly mark the location of the TV near the cloud top, where the strongest vorticity and closed streamlines are found. Figures 1c and 1d suggest that the TV was generated by the strong updrafts in the core that formed the curl and vorticity. The second row in Figure 1 presents the second simulated cloud, which has a more complex structure. In Figures 1f–1h, we can observe the development of a second turret (formed by another bubble) emerging on the left side of the highest cloud top (centered at $x = 2{,}200$, $z = 1{,}000$ m).

Our high-resolution simulated cumulus cloud results demonstrated a more complex structure of a TV than an axisymmetric ring vortex, as was also shown with direct numerical simulations of dry thermals (Lecoanet & Jeevanjee, 2019). This difference will be discussed next; Cumulus cloud TV will be referred to as CuTV hereafter. Figure 2 shows normalized vorticity (ζ) and velocity vectors of the first cloud presented in the upper row of Figure 1 at three averaging scales for snapshots taken at two different time instants. The cloud appeared after 20 min of simulation time and reached its maximum development at 33 min. The upper row in Figure 2 presents the cloud at 31 min of simulation (11 min in the cloud lifetime) during the growth stage, and the second row is at 33 min (the mature stage, at which the cloud reached its maximal top height). The first column (Figures 2a and 2d) presents the wind and vorticity data at a 10 m resolution. In the second and third columns, the velocity field is

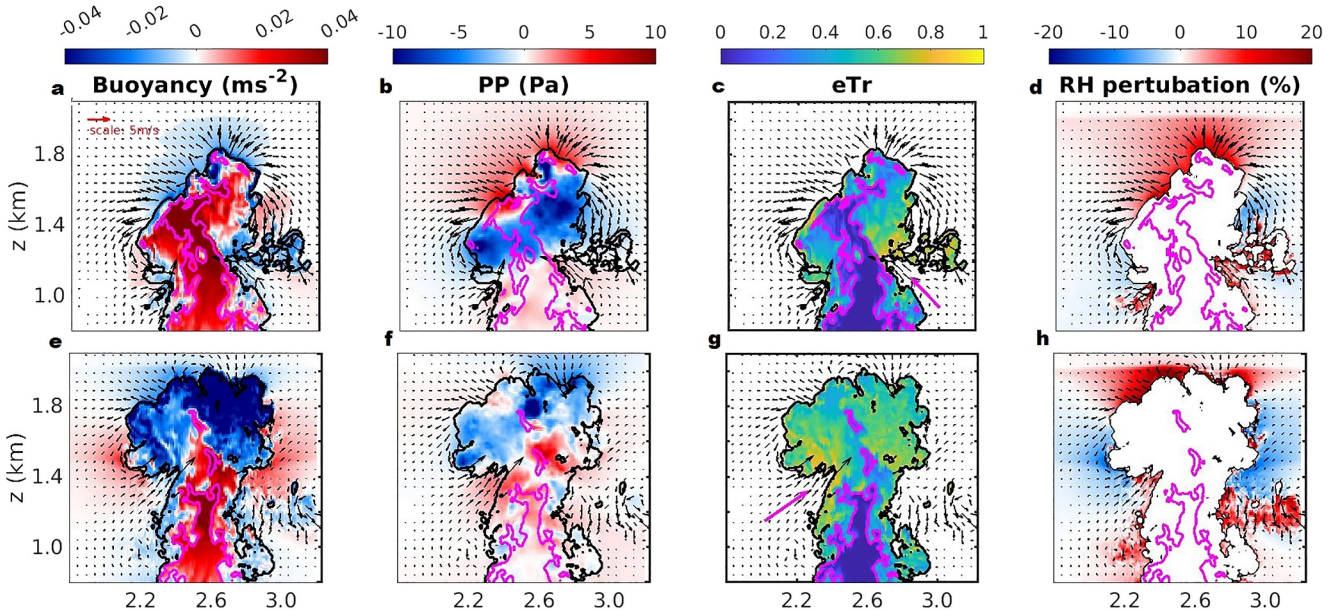

Figure 3. *Macro-physics of the toroidal vortex* (TV). *x-z* cross sections of cloud macro-physical fields with a black contour marking the cloud edge ($ql = 0.01$ gkg^{-1}), a magenta contour for the core (normalized sub-cloud tracer = 0.8), and black arrows representing the velocity field smoothed with a 410 m filter (see red arrow in panel (a) for scale). *First row*—The first cloud (from Figure 1a) during its growth stage at 31 min of simulation. (a) Buoyancy—the driving force of the vortex. (b) Pressure perturbation (PP) with a high anomaly on the cloud top and two low PP spots in the center of the vortices. (c) A normalized environmental tracer (eTr) inside the cloud (high values indicate entrainment). The magenta arrow points to the region where the TV entrains air deep into the cloud. (d) The relative humidity anomaly compared to the far environment profile. *Second row*—Same as the first row but for the first cloud at 33 min at its mature stage.

averaged in the horizontal direction with 110 and 410 m filters, respectively. Examining the flow patterns under different averaging scales and at two different time points indicated interesting CuTV dynamics. At 31 min in simulation time, the cloud was still in the developing stage. A clear structure of the TV was present on both sides of the cloud (magenta stars mark the vortex center), in the raw velocity field (Figure 2a), and in the averaged velocity fields (Figures 2b and 2c). This was not the case when the cloud reached its mature stage 2 minutes later. At 33 min, the TV was evident only on the left side of the cloud (marked by a magenta star), demonstrated by the 10 m resolution data, as shown in Figure 2d. Averaging the flow with a 110 m filter shows that the right (red) side of the cloud consists of a few smaller-scale eddies (red ζ spots, Figure 2e). Considering that 2 min earlier, this area in the cloud was a large coherent vortex (as shown in Figures 2a–2c), suggests that the difference between Figures 2b and 2e represents the stage of the vortex breakup into smaller vortices. Averaging on a larger scale of 410 m seems to recover the parent TV in the form of the mean flow. The dynamics of the cloud, thermals, and CuTVs that are mentioned above are visualized in Movies S1 and S2.

Next, we investigated the forces driving the formation and evolution of the CuTV. Figure 3 presents a zoom-in of the cloud and the CuTV at 31 and 33 min of simulation (top and bottom row, respectively) with black arrows marking the wind field, averaged using a 410 m filter. Figures 3a and 3e present the buoyancy field with the cloud core marked by a magenta contour of $cTr = 0.8$. The buoyancy was calculated as the deviation of the virtual potential temperature from the sounding profiles used to initiate the simulation. The core of the cloud is warmer than its surrounding environment due to the source of its air (lower levels) and latent heating. The buoyant region of the cloud was characterized by strong updrafts that caused a horizontal wind shear $\left(\frac{dw}{dx}\right)$ that drove the CuTV. Figure 3b presents the pressure perturbation (PP) field, which shows a positive anomaly at and above the cloud's top, acting as an opposing force to the upward-moving air. This positive PP formed as the cloud pushed its way up through the still air. Another interesting insight gained from the PP field was the two low-pressure spots located at the vortex center (on both sides), in agreement with the flow field around them. These low PP spots are expected to form in the center of a vortex and, thus, are markers of the coherent parts of the CuTV that are independent of the velocity field filtering analysis. Here we note that the penetration of the cloud through the inversion layer at 1,500 m intensifies the vortex, nevertheless, it appears also below the inversion in earlier stages of the simulated

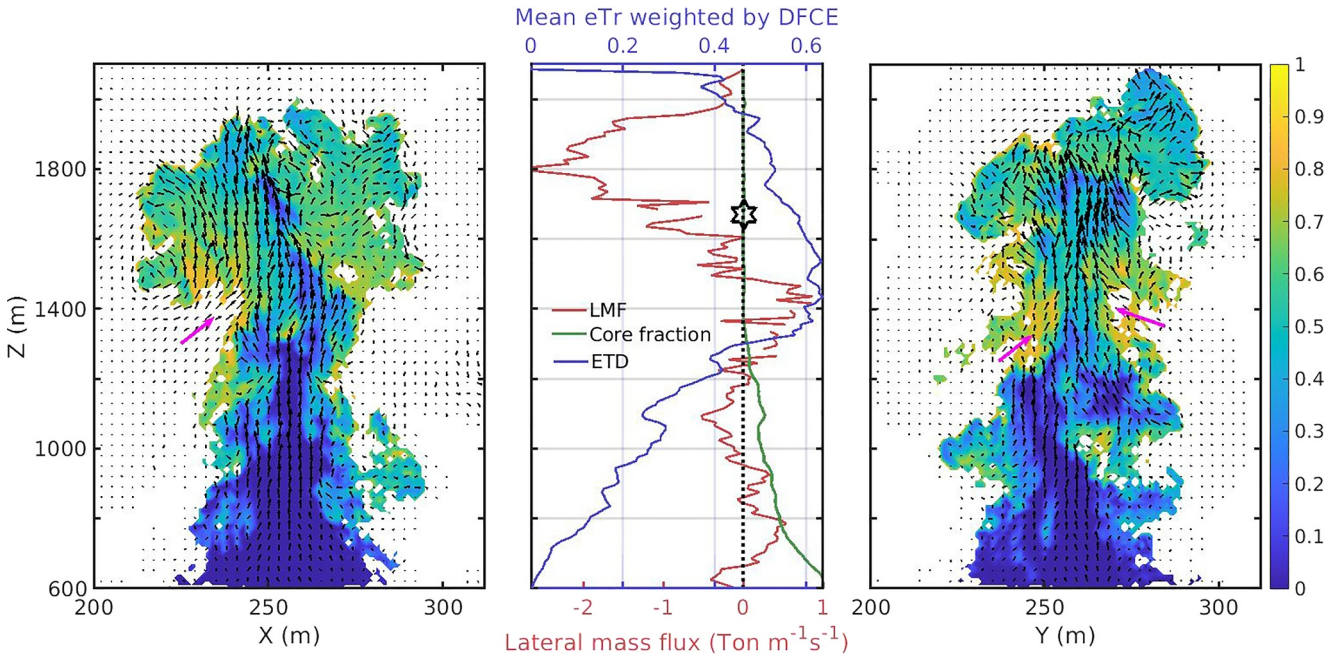

Figure 4. *Profiles of toroidal vortex* (TV) *entrainment estimators*. (a) *x-z* cross-section of *eTr* inside the cloud at 33 min. Magenta arrow marks the entrainment region driven by the TV. (b) The red curve is the lateral mass flux, peaking at the cloud-top detrainment zone and near the bottom of the vortex (same layer as indicated by the magenta arrows in neighboring panels). Black hexagram points to the altitude of the maximal filtered updraft that represents the center of the vortex. The blue curve is Entrained Tracer Depth (the mean *eTr* weighted by distance from cloud edge), illustrating where the tracer is entrained deep into the cloud, and the green curve is the core ($cTr > 0.8$) area fraction ranging between 0 and 1 (corresponding to the bottom *x*-axis but dimensionless). (c) Same as (a) but on the *y-z* plane.

clouds and in another cloud realization constructed from a radiosonde measured at Hawaii (Heiblum et al., 2019) with a higher inversion (see Supporting Information S1).

Examining the CuTV effects on the properties of the cloud and its near environment yielded interesting insights. Figure 3c presents a cross-section of *eTr* inside the cloud during its growth stage. A narrow yellowish band at the cloud edges indicating large *eTr* values showed that environmental air was mixed into the cloud throughout its entire periphery. This edge region is the transition zone discussed in Eytan et al. (2022), and its formation can be explained by diffusion of small-scale turbulent mixing (Pinsky & Khain, 2023). The location of the strongest lateral airflow into the cloud (driven by the CuTV) is marked by a magenta arrow that also points to significant penetration of environmental air into the cloud (as identified by hot spots of *eTr*). This penetration reached the center of the cloud, causing the narrowing of the core and its breakup into small fragments in the upper part of the cloud.

Figure 3d presents the deviation of the relative humidity (RH) near the cloud from the far environmental RH profile. One can see that the horizontal divergence near the cloud top detrained cold and humid air (due to evaporation) into the surroundings. It increased the RH above the cloud by ∼10%. Previous studies suggested that a humid subsiding shell driven by negative buoyancy forms around the cloud and decreases the mixing-evaporation effects by isolating it from the environment (Heus & Seifert, 2013; Romps, 2010). Here, it was shown that despite the humidification near the cloud top, the downdrafts outside the upper part of the cloud were drier than the environment, as they originated in the drier layers above and were subject to adiabatic heating. Moreover, Figures 3a and 3e showed that the outside air experienced downward movement despite its positive buoyancy, probably because it was driven by the momentum of the CuTV and pressure gradient forces which in this case are intensified by the penetration of the inversion. This portrayed a different picture from the common paradigm depicting a humid-subsiding shell driven by evaporative cooling and negative buoyancy (Heus & Jonker, 2008; Katzwinkel et al., 2014). Note that most in situ measurements are taken near clouds' tops. This raises the question of whether the reported downdrafts near cloud tops in field campaigns are caused by purely buoyancy-driven subsiding shells or whether they represent a part of the CuTV flow. We note that evaporation at the cloud top, generating a subsiding shell, can support and enhance the CuTV. We do not present here the

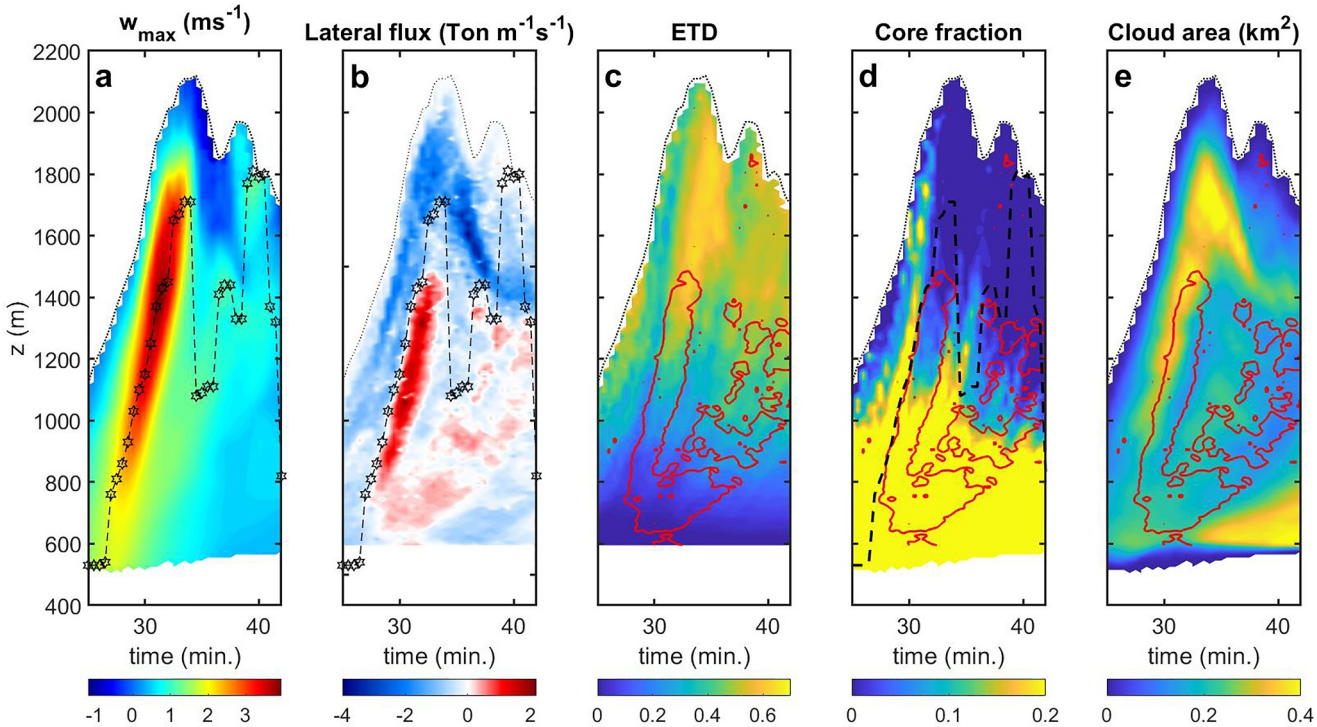

Figure 5. *Entrainment estimators and the toroidal vortex* (TV) *in z-t space*. The time evolution of the profiles presented in Figure 4. (a) Maximal filtered updraft (w_{max}) in each vertical level. The dotted curve marks the cloud top, and a hexagram curve depicts the cloud's w_{max} level. The filter size is 400 m on the horizontal and 50 m on the vertical. (b) Lateral mass flux with the domain's w_{max} as a hexagram curve for estimating the ascent of the TV center. (c) Entrained tracer depth ($ETD_{(z)}$) is the vertical profile of the mean *eTr* weighted by distance from the cloud edge. Red contours mark entrainment regions (marked in red) from panel (b). The contours exhibit how the increased entrainment driven by the vortex is responsible for increased environmental air deep in the cloud. (d) Cloud core area fraction (core is defined at $cTr > 0.8$) with red contours as in panel (c) and a dashed black line representing the w_{max} curve from panel (a) (hexagrams were removed for clarity). (e) Cloud area profile.

temperature and specific humidity perturbation fields because the temperature perturbation field is closely proportional to the buoyancy field in Figures 3a and 3e; the same is true for the specific and RH fields (Figures 3d and 3h).

Eventually, examining the RH field (Figures 3d and 3h) showed the effect of the CuTV on the entrained air to be qualitatively similar to the assumed effect of the subsiding shell. It is shown that the entrainment caused by the CuTV is of humid air compared to the far environment as can be seen from the red colors of the entrainment regions (see areas of magenta arrows in Figures 3c and 3g for example). This is quantified in the next section using the Lagrangian tracers. The questions arising from the results in this section are: What is the contribution of the CuTV mixing to the total mixing and dilution of the cloud? Does the CuTV recirculate the cloudy air detrained from the cloud top back into the cloud? These questions are answered in the next section.

4. The Toroidal Vortex Role in Cloud Mixing With Its Environment

In this section, we quantify the cloud mixing using the method described in Section 2.4. Figures 4a and 4c show two perpendicular cross sections on the *x*-*z* and *y*-*z* planes, at the center of the domain, for the first cloud in Figure 1, during its mature stage (at 33 min). The colors represent *eTr* inside the cloud, where dark blue represents the undiluted cloud core, and highly mixed regions are marked in yellow. The velocity field at a 10 m grid spacing is marked by black arrows. Figure 4b presents the vertical profile of the LMF (red curve) as a measure of mixing (see Section 2.4). The profile shows a large negative peak at the upper third part of the cloud, marking the detrainment near the cloud top. This is the largest flux along the profile, in agreement with Zhao and Austin (2005b) and Dawe and Austin (2011). The profile also points to two inflow layers of environmental air into the cloud (positive values); one just above the cloud base, around 700 m, and another at approximately 1,400 m. The

entrainment level above the cloud base was observed in other studies and explained by Heus et al. (2009) as a consequence of a weak inversion layer (convective inhibition layer) that lies just above the cloud base. The second in-cloud flux peak (near 1,400 m) is intriguing, as the cross sections in Figures 4a and 4c suggest that this intense influx can be explained mainly by a large-scale vortex, that is, the CuTV (magenta arrows are provided to guide the eye). The upper part of the *LMF* profile presents the structure of the CuTV—bounded from above by a peak in detrainment near the cloud top and intense entrainment from below. Such a profile agrees well with numerical simulations of ring vortices (Sau & Mahesh, 2007) that showed good comparison to lab experiments (Gharib et al., 1998). Observations (Damiani et al., 2006) and analytical ring vortex solutions (Hill, 1894) suggested that the maximal vertical velocity should be found in the center of the vortex (a 3D ring vortex). In Figure 4b, we plotted a black hexagram at the altitude of maximal vertical velocity (the original velocity field was filtered with a 410 m window, as in Figure 2f), and $LMF = 0$ (the $LMF = 0$ coordinate was chosen only for the presentation and didn't have a physical meaning). This seems to approximate the center of the CuTV well. Figures 4a and 4c also show an important relationship between the CuTV and the entrainment of environmental air deep into the cloud. One can see that the magenta arrows, which mark the CuTV in-cloud flux, also point to the increased *eTr* region inside the cloud. While the small-scale turbulent diffusive mixing increases *eTr* on the edge of the cloud, the large-scale flow related to the CuTV entrains air deep into the cloud. In order to quantify this phenomenon and relate it to CuTV, we calculated the Entrained Tracer Depth (ETD) as

$$ETD_{(z)} = \sum_{1}^{N} eTr_i \frac{DFCE_i}{\sum_1^N DFCE_i} \tag{2}$$

where *DFCE* is the distance from the cloud edge as calculated by Eytan et al. (2022). It is the Euclidean distance of each point in space to the nearest cloud edge point (with cloud volumes defined where liquid water mixing ratio >0.01 gkg^{-1}). Equation 2 is the mean *eTr* of each layer weighted by its DFCE (i.e., horizontal depth in the cloud). *N* is the number of cloudy points at each altitude, and *i* is the summation index. *ETD* exhibits higher values for regions in the cloud in which environmental air penetrated deep into the cloud. The blue curve in Figure 4b is the $ETD_{(z)}$ profile. It shows an almost linear increase from 0 to 0.4 up to $z \approx 1{,}300$ m, suggesting a constant dilution rate of the cloud and its core at this layer. At $z = 1{,}300$ m, the altitude of the CuTV entrainment layer, a sharp increase of 50%, is observed in *ETD*, which reaches its peak value (0.6) in less than 100 m. This value is almost constant along the CuTV entrainment layer and then decreases with altitude back to zero. The relationship between the *ETD* and *LMF* and their co-location with the CuTV point to the dominance of the CuTV in the mixing of a developing Cu. Another way to demonstrate the important role of the CuTV in mixing is by showing its impact on the undiluted core of the cloud. The green curve in Figure 4b is the area fraction of the cloud's core as a function of altitude, where the core is defined by $cTr > 0.8$ ($\sim eTr < 0.2$). Note that it corresponds to the bottom *x*-axis but that it is dimensionless. It shows that the CuTV entrainment level acts to reduce the core fraction to nearly zero and explains similar profiles presented in Eytan et al. (2022).

Figure 5 shows the evolution of the profiles presented in Figure 4b for the same cloud by plotting the variables on a *z*-*t* space (Hovmöller diagram) using a temporal resolution of 30 s Figure 5a presents such a plot for the maximal filtered updraft per altitude (w_{max}) with a hexagram curve that marks the maximal updraft in the cloud. This curve represents the movement of the CuTV's center, as in Figure 4b. Figure 5b presents the *LMF* and the cloud's maximal updraft curve, as presented in Figure 5a. The CuTV circulation is demonstrated by a blue band near the top of the cloud (a zone characterized by detrainment) and a red (entrainment) band just below the vortex center, represented by the hexagrams. The vortex occupies the upper third of the cloud and ascends together with the cloud top. Sherwood et al. (2013) explained this constant ascent of the cloud's top and CuTV as a balance between the buoyancy and the PP gradient force acting as a drag force on the upward-moving cloud.

Figures 5a and 5b show one dominant bubble (thermal) as a pulse of updraft with its corresponding CuTV; as the bubble dissipates and loses buoyancy, the cloud top begins to descend. While the first pulse reaches the inversion (at 1,500 m), a second one arises (shown by a new maximal updraft above an entraining layer at $t = 33.5$ in Figure 5b). The second updraft pulse and the decreasing cloud top converge around the inversion to form a strong horizontal divergence (detrainment), as observed by the dark blue colors at the maximal altitude of the second pulse. This strong detrainment rate was also described and explained similarly by Zhao and Austin (2005b) for three representative clouds in a cloud field. Figure 5c shows the same plot for *ETD* with the entrainment regions from Figure 5b marked by a red contour of $LMF = 0.05 \frac{Ton}{ms}$. It demonstrates how the air entrained by the CuTV

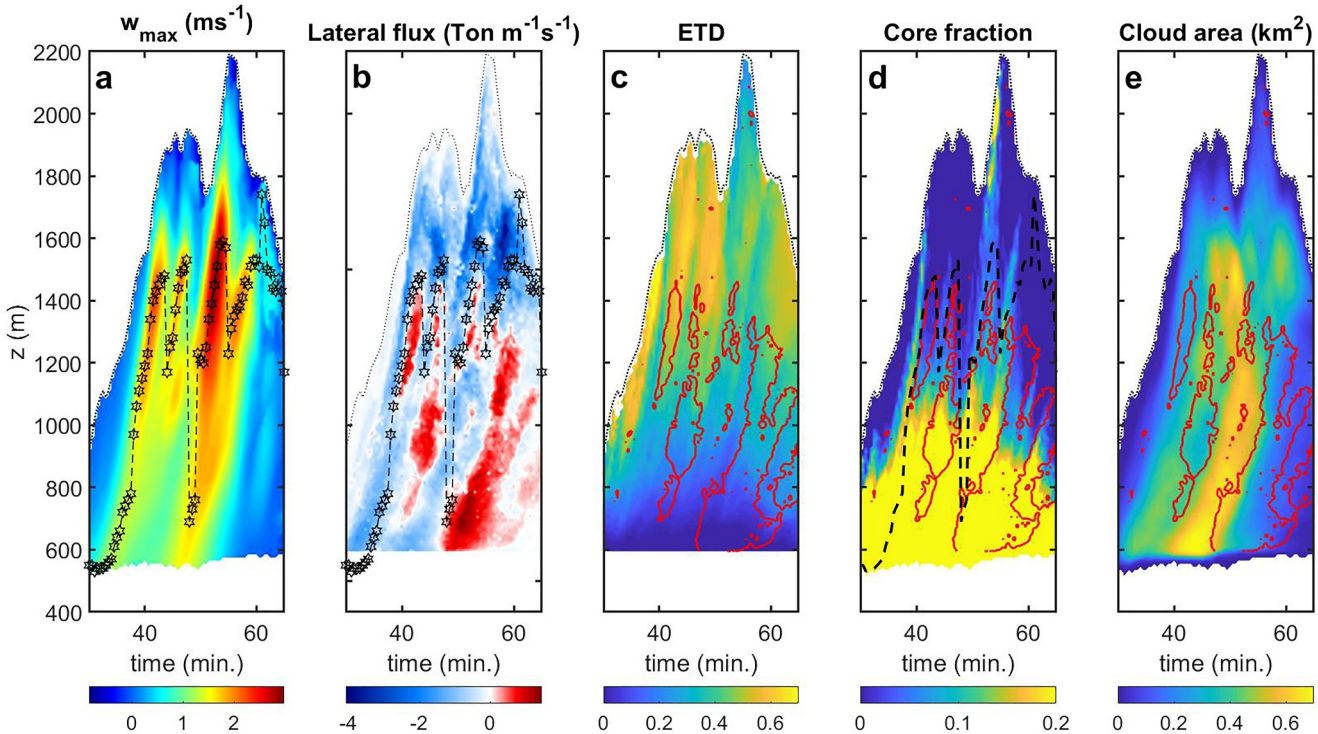

Figure 6. *z-t space of entrainment estimators for the second* (*multi-bubble*) *cloud*. Same as Figure 5, but for a cloud realization comprised of several bubbles and their corresponding toroidal vortices.

penetrates deep into the cloud. The *ETD* value rises to ~0.6 at $t = 32$ min and $z = 1{,}300$ m, which is the height of maximal entrainment in Figure 5b. The imperfect match between *LMF* and *ETD* in Figures 4b and 5c probably results from the fact that *LMF* measures entrainment on the cloud edge, while *ETD* measures entrainment deep in the cloud. Hence, there is a delay in the *ETD* response, expressed by a delay in both time and vertical dimensions.

Figure 5d presents the undiluted core area fraction with the entrainment regions marked in red contour and the domain's w_{max} by black dashed lines (hexagrams were removed for clarity). It demonstrates that the regions of updraft pulses in Figures 5a and 5b (black hexagrams) can be characterized as relatively undiluted bubbles. Notably, the correlation in altitude and time between w_{max} and the core area fraction is solid only up to the inversion layer, while above it, the w_{max} curve is located below the regions of high core area fraction. This seems to mainly result from the filtering analysis that averages the updraft field in space. Plotting the w_{max} curve while using a filter size smaller than 400 m yields a better agreement between the curve and the core fraction field—but leads to a noisier curve (not shown). Figure 5d also shows how the entrainment caused by the CuTV (red contours) acts to decrease the core size. The core decay corresponds to the end of the CuTV's life cycle since the core and its strong buoyancy and updrafts are the generators of the CuTV. When the core dissipates, the source of vorticity diminishes, and the CuTV eventually breaks down into smaller eddies and dissipates as well. Figure 5e presents the evolution of the cloud area's vertical profile. It is evident the CuTV, with its corresponding entrainment/detrainment, controls the cloud's shape. In locations and times where horizontal divergence and detrainment dominate, the cloud area increases, while the entrainment zones (red contours) decrease the cloud area due to convergence and evaporation. This is another way to explain the mushroom-like shape of the cloud.

Figure 6 is similar to Figure 5 but presents the results for the second (more complex) cloud comprised of a succession of bubbles (the 2nd cloud from Figure 1). Surprisingly, the simplified view of the CuTV holds also for this more complex cloud. The only observed difference is the relationship between the cloud area and *LMF* (which is weaker for the second cloud), probably due to the interaction between the different bubbles. In this case of cloud realization (that started with weaker updrafts), two weak bubbles seemed to locally moisten the environment and preconditioned the environment allowing the third bubble to reach a higher cloud top that is similar

to the first cloud's top. This is demonstrated well by the vortex center curve (maximal updraft) in Figure 6b and by the large area fraction of the core at high altitudes (Figure 6d). The comparison of the two clouds shows that in our case, the cloud depth is controlled by thermodynamics and large-scale conditions (determined in the model by prescribed surface fluxes, subsidence, and heating and moistening tendencies). Nevertheless, the clouds' lifetime (see the *x*-axis) and width (see color-bar of Figure 6e) are different in the two realizations. Hence, the initial perturbation and the dynamics of the bubbles and their CuTVs also play an important role. Figure 6 also suggests that the CuTV might explain the pulsating behavior of Cu that was observed and investigated in earlier studies (Damiani et al., 2006; Heus et al., 2009; Moser & Lasher-Trapp, 2017; Zhao & Austin, 2005a). As the CuTV erodes the undiluted core, it breaks it into smaller fragments. These fragments ascend and can be considered as bubbles or thermals.

Experimental studies of ring vortices show that the ring vortex properties (and the injected fluid they dilute) depend on the stroke ratio, which is the length of a column of fluid injected through an aperture, divided by its diameter (Dabiri & Gharib, 2004; Gharib et al., 1998; Sau & Mahesh, 2007). Later studies have demonstrated that the aspect ratio of perturbation, which is equivalent to stroke ratio, highly affect the spreading and dilution rate of the thermal (Lai et al., 2015; Morrison et al., 2023). Note that an equivalent parameter in clouds should be closely related to the cloud aspect ratio, but larger, due to the capping inversion that limits the cloud growth and considering the continuous supply of updrafts coming from below the cloud base. Sau and Mahesh (2007) used direct numerical simulations of TVs generated in the lab (Dabiri & Gharib, 2004; Gharib et al., 1998) to study the important role of ring vortices in diluting a volume of fluid injected into a medium. They demonstrated that a trailing fluid column is formed below the ring vortex, and the dilution efficiency of the fluid is reduced when the stroke ratio exceeds ∼3.5. They concluded that to maximize dilution efficiency, several pulses of ring vortices with a small stroke ratio (i.e., aspect ratio) should be generated. Here we suggest that their conclusion implies that the pulsating behavior of Cu clouds acts to oppose the vertical transport of convective clouds with a high aspect ratio by increasing dilution efficiency.

The next question to be answered is whether the CuTV recycles the cloudy air back into the cloud. In other words, what fraction of the air entrained by the CuTV originated from the upper parts of the cloud? Since the Eulerian framework treats all air as a bulk, we turned to the Lagrangian tracers (described in Section 2.3). The Lagrangian analysis was conducted on a third simulation (i.e., realization) of a cloud in which the output data was recorded every 2 s. The *z*-*t* space of *LMF* for this cloud is presented in Figure 7a and the CuTV's entrainment layer was defined every 30 s as the layer of positive values of *LMF* around the maximal peak in the profile (represented by two black lines marked in Figure 7a). The trajectories outside the cloud for all Lagrangian tracers that entered the cloud in those layers were analyzed. They were separated into "cloudy tracers" if they exited the cloud before re-entering it, and "Environmental tracers" for the ones that entered the cloud for the first time. The difference in altitude was calculated for each tracer as $\Delta z = z_{in} - z_0$, where z_{in} is the entrance altitude, and z_0 is the exit altitude for cloudy tracers and the initial altitude for environmental ones.

A total of 11,281 tracers entered the cloud in the chosen layer, but many of them showed a small Δz and a short lifetime before re-exiting the cloud or a small lifetime in the environment before re-entering. This behavior does not fit the structure of the CuTV and was attributed to small-scale turbulent motions, such as the mixing process at cloud edge that forms the thin transition zone. These turbulent motions were disregarded from the analysis by excluding tracers with $\Delta t < 1.5$ min between re-entering or re-exiting the cloud (Appendix A supports the choice of this threshold). Figure 7b shows the histogram of Δz outside the cloud for the 8,996 analyzed tracers. 92% of the tracers were identified as "Environmental," and only 3.7% were "Cloudy" with $\Delta z \leq 0$ (which is expected from the flow pattern created by the CuTV). This means that only 3.7% of the particles represent air that was recycled by the CuTV. We note that while the downdrafts outside the cloud were in the order of -1 ms^{-1} (Figure 3a), the vortex ascended at a rate of ∼3 ms^{-1} (according to the gradient of the vortex center in Figure 5a). It follows that the tracers' Δz values should be smaller than the real size of the vortex ∼400 m and equal to or larger than zero in absolute values (see Figure A1 in the appendix). 42% of the tracers that entered the cloud in the entrainment layer (at the lower part of the CuTV) were found to originate below the entrainment altitude ($\Delta z > 0$). Including the tracers affected by small-scale turbulent motions in the analysis (i.e., by not using the time-scale threshold) yielded fairly similar shapes of the Δz distributions (and *RH*, discussed below). However, the "cloudy' tracers" portion increased to 18% with a corresponding increase in "Cloudy" tracers with $\Delta z \leq 0$ to 7.5%.

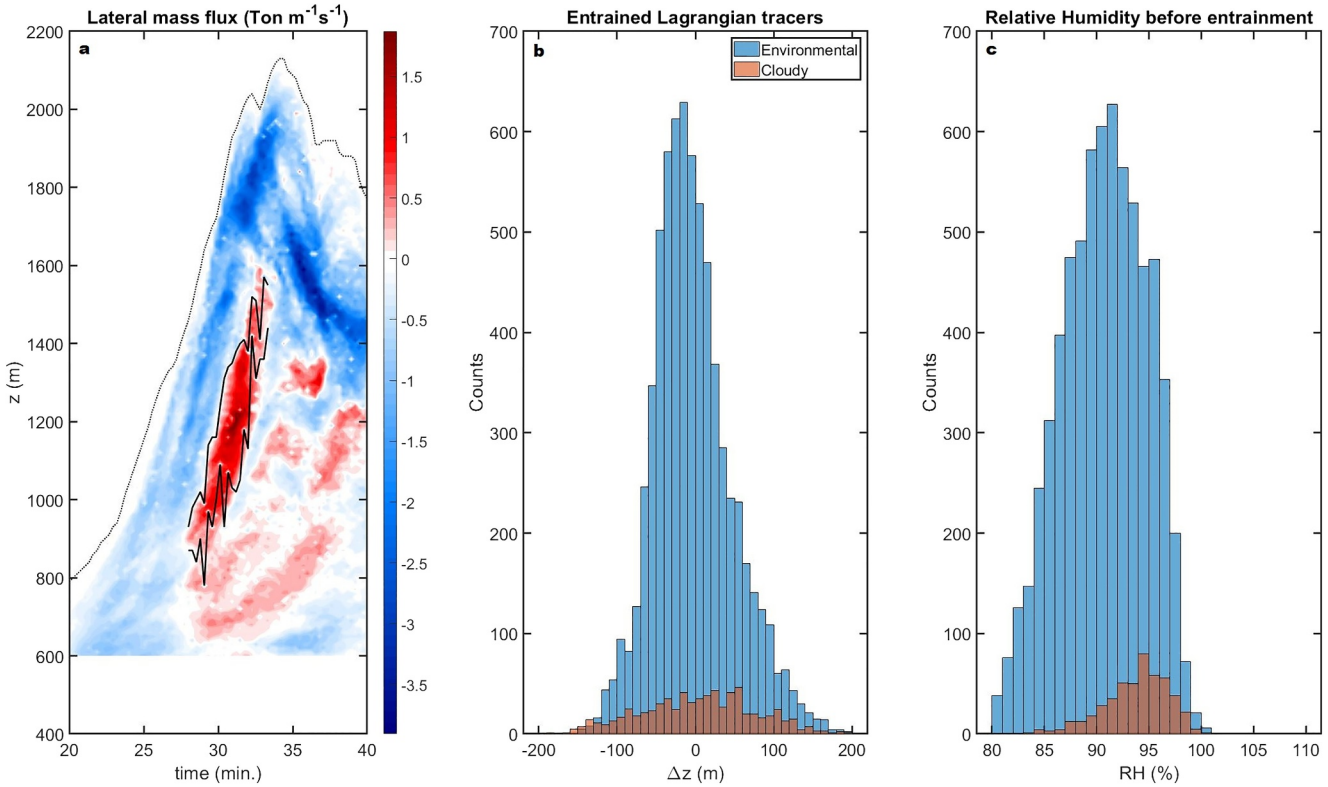

Figure 7. *Tracking the origin of air entrained by the toroidal vortex* (TV). Analysis of Lagrangian tracer trajectories that entered the cloud at the entrainment layers driven by the TV. (a) Same as Figure 5a for the cloud realization on which the Lagrangian analysis was conducted. Entrainment layers marked by black lines were defined by the maximal entrainment in the profile and all other levels with a positive sign above and below it. (b) A histogram of the altitude difference for all particles that entered the cloud in the layers marked in panel (a), separated into recycled tracers that re-enter the cloud (red) and environmental tracers (blue). (c) Same as (b) but for the relative humidity of the air just before entering the cloud (i.e., the point with a distance of 10–20 m before the penetration into the cloud).

These intriguing results show that most of the air entering the cloud in the entrainment layer is a mixture of environmental air with some older cloud remnants and was not recycled by the CuTV. It means that the vortex's instantaneous image in the velocity field can be deceiving as a particle doesn't follow the streamlines. One explanation could be that the changes in the velocity field were faster than a particle's lifetime in the vortex or the time it took a particle to complete a considerable distance in the vortex. Another explanation would be that the CuTV is part of a PP and flow fields that formed as the cloud developed, acting to increase the entrainment of environmental air. This is partly shown in Figures 3b and 3f, where some of the arrows in the entrainment layers originate from lower altitudes. Apparently, the low PP pattern built by the CuTV acts to suck environmental air from the same altitude or several tens of meters below.

The Eulerian perspective in Figures 3d and 3h suggests entrainment of humid air, but it also shows that the air detrained by the CuTV could be drier than its surroundings while descending. Hence, we turn to examine the RH with which the entrained air entered the cloud. We interpolated the RH value in 3D at the position of each Lagrangian tracer, just before it entered the cloud (at a distance of 10–20 m from the cloud edge, equivalent to a few seconds of tracer movement). The histograms of RH values for the "Environmental" and "Cloudy" tracers are presented in Figure 7c. It is shown that the "Cloudy" tracers enter the cloud with a median RH of 94%. Notably, in such high RH conditions, homogeneous and inhomogeneous mixing are indistinguishable using the common mixing model that is used in the study of the effects of mixing on microphysics (Baker et al., 1980; Lehmann et al., 2009). The "Environmental" tracers comprising most of the data (92%) are drier than the "Cloudy" ones, but nevertheless, show high RH values as well, with a median of 90%. These results show that despite the relative drying of descending detrained air and the dominant entertainment of environmental air, eventually, the entrained air is more humid than the far environment (with environmental RH decreasing from 90% at cloud base to ~80% at the top of the cloud layer). Figures 3d and 3h suggests that this is due to the intense evaporation occurring on the edges of the cloud at the entrainment layer, a region that environmental air that is entrained by the vortex has to

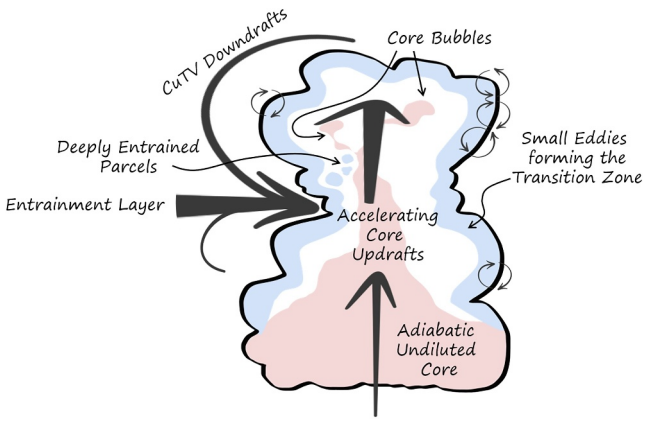

Figure 8. *Schematic picture of the structure of a growing cumulus cloud.* As the cumulus cloud grows, its undiluted core contains the highest updrafts, with adiabatic thermodynamic and microphysical properties (light red). Small-scale mixing at the edge of the cloud entrains environmental air by turbulent diffusion and constructs the transition zone (light blue, 10s of meters wide). This region is characterized by sharp thermodynamic and microphysical gradients with weak updrafts and even downdrafts. A CuTV is formed in the upper part of the cloud with strong detrainment flux from the cloud top. The entraining part of the CuTV, located 100s of meters below the cloud top consists mostly of environmental air from this level and below, and the cloud's top layer (note that the width of the arrow indicates the partial contribution to the entrainment fluxes). This air is mixed with the transition zone's air and with the humid shell to some extent. The CuTV entrains air deep into the cloud (illustrated by the blue blobs inside the cloud) to form large diluted volumes (white region) and erodes the core into small core fragments (i.e., bubbles).

cross and get mixed with. This brings up an interesting point regarding the Lagrangian analysis. The Lagrangian particles are tracked using the velocity field (and are defined as environmental from this point of view), nevertheless, along the trajectory their properties (e.g., RH) are mixed with air that was moistened by the cloud, hence they also hold cloud information to some extent.

5. Conclusions

Despite decades of research, the process of mixing in cumulus clouds (Cu) is still poorly understood. The questions it raises are important not only for the cloud physics community that desires to better understand clouds; It is also pivotal for weather and climate prediction, as the parameterizations of Cu clouds and their mixing are one of the main sources of uncertainty in large-scale models. Figure 8 gives a schematic picture of the cloud's structure that arises from a compilation of this work with a few others (Arieli et al., 2024; Eytan et al., 2021, 2022; Pinsky & Khain, 2023; Pinsky et al., 2021, 2022).

5.1. Defining the Toroidal Vortex in Cumulus Clouds

In this study, we used high-resolution Large eddy simulations (10 m) to investigate the TV that developed near the top of growing shallow cumulus clouds (a vortex in the scale of 400 m in our case study of BOMEX clouds). Such unique simulations enabled us to resolve the TV with great detail. The TV of a cumulus cloud (CuTV) was shown to exist in previous studies by observations (Damiani et al., 2006; Wang & Geerts, 2015) and modeling (McKim et al., 2020; Romps & Charn, 2015; Sherwood et al., 2013; Zhao & Austin, 2005b). The CuTV is more complex than a common ring vortex as it spans a wide spectrum of turbulent scales and includes microphysical processes that provide feedback on the dynamics (mostly by latent heat release, Morrison et al., 2021; Vybhav & Ravichandran, 2022). Moreover, part of the complexity is due to the nature of a convective cloud ascending in a varying medium (e.g., decrease in pressure and inversion layers) with a highly turbulent background. In this study, we demonstrated how the detection and definition of CuTV depended on the scale of analysis and the stage of the vortex and cloud life-cycle. During the early stages of cloud development, the CuTV appeared as a clear and coherent structure. As the cloud develops into its mature stage, the vortex starts to break down into smaller vortices that dissipate at various times and lose its coherent structure. Nevertheless, low-pass filtering (e.g., moving average) enables the recovery of the "parent" coherent vortex. Hence, during the dissipation stage, the CuTV is not an axisymmetric 3D feature (like a common ring vortex), but rather a statistical feature. This life-cycle of the CuTV can produce complexity when describing the dynamics of the cloud top ascent and its mixing (Figure 2). Differences between a basic ring vortex and the CuTV were also shown in recent work by Pinsky et al. (2023) that compared a Cu cloud simulated as the clouds analyzed in this work, with a Hill vortex solution (Hill, 1894). They found that while several properties were comparable, others held biases. Nevertheless, when estimating the mean AF (a measure of cloud mixing state) of the ascending bubble vortex, they obtained a value of 0.4, which is in remarkable agreement with laboratory experiments (Dabiri & Gharib, 2004) and direct numerical simulations (Sau & Mahesh, 2007) of basic ring vortices.

The CuTV is shown to ascend together with the cloud top at a constant velocity, demonstrating the strong link between the two parts of a buoyant bubble (the cloud top and the vortex). This was presented in earlier works and explained to be a consequence of a balance between buoyancy and PP gradient force (Romps & Charn, 2015; Sherwood et al., 2013). Here, we point to the importance of the CuTV's feedbacks on those fields. While the horizontal gradients in buoyancy and related updrafts are the sources of vorticity generating the CuTV, the CuTV acts to diminish the undiluted buoyant core by entraining environmental air deep into the cloud, hence, eliminating its own source. The CuTV is also driven by the PP above and below it, but at the same time, it generates regions of low PP in its center (see Figures 3b and 3f). The location of these low PP volumes could serve as an

indication of the coherent parts of the vortex. The low PP volumes may be an efficient tool for defining and tracking the TV in 4D fields in future studies, in addition to the flow field filtering methodology used here.

5.2. The Role of the CuTV in Cloud-Environment Interactions

Section 4 established the important role of CuTV in cloud mixing with its environment. Direct calculations of the lateral mass flux (*LMF*; see Equation 1) through cloud edges showed a strong outflow (detrainment) at the cloud top and a dominant inflow (entrainment) several hundred meters below it. Moreover, the maximal average (filtered) updraft (representing the center of the 3D vortex) was located between the two regions of entrainment and detrainment. The *LMF* profile revealed that the complex structure of the cloud with its CuTV could be represented in a simplified way by a 1D profile. In this profile, the top of the vortex (and the cloud) detrains air while its bottom part entrains. An Eulerian passive tracer was added to the simulated cloud environment (*eTr*) to be used as an accurate measure of the cloud dilution and mixing with its environment. A measure of the mean *eTr* weighted by its horizontal distance into the cloud (*ETD*) was calculated for each vertical layer to show how deep the *eTr* penetrated the cloud. The *ETD* profile agreed with the location of the CuTV influx layer, demonstrating that the CuTV advected air deep into the cloud. The penetration of environmental air deep into the cloud acts to erode the core and decrease the area fraction of the entire cloud. This is an important role of the CuTV as the core is the source of the cloud's condensate and updrafts, dictating the vertical mass flux. The erosion of the core marks the beginning of the cloud's dissipation stage and the end of the CuTV generated by the updrafts. This negative feedback is equivalent to rain initiation in deeper precipitating clouds.

The simplified 1D structure obtained by profiles of different measures of mixing for a "single-bubble" cloud was shown here to hold also for a more complex cloud consisting of several pulses (Figure 6). The pulsating behavior of Cu was addressed in previous Cu dynamics and thermals studies (Damiani et al., 2006; Heus et al., 2009; Morrison et al., 2020; Zhao & Austin, 2005a). Figure 6 suggests that this behavior could be explained by the CuTV evolution. The CuTV drives a strong and deep entrainment that erodes the undiluted core and breaks it into fragments in the upper part of the cloud. The additional supply of undiluted cloudy air from below, with its vertical momentum, forms a new convective pulse, generating a new CuTV that would eventually erode the core again. This could explain the oscillating (pulsating) behavior. Simulations of lab-generated toroidal vortices suggested that pulsating behavior is more efficient in diluting the injected fluid (Sau & Mahesh, 2007). These results, combined with the description of the cloud's CuTV-core interaction from the paragraph above, suggest that the pulsating behavior of cumulus clouds opposes the vertical fluxes of convection (i.e., injected surface air).

5.3. The Origin of Air Entrained by the Vortex

Finally, we explored the trajectories of Lagrangian particles that entered the cloud at the entrainment layer driven by the CuTV (selecting only the trajectories that represented motions with a time scale of the CuTV). The analysis showed that 92% of the particles that entered the cloud in the entrainment layer originated in the environment. Only 4% of the entrained tracers originated in the cloud itself at higher altitudes (i.e., recycled by the CuTV, as expected in a closed circulation vortex flow; see Figure 7). This means that most of the tracers did not follow closed vortex streamlines, as displayed in a snapshot of the flow field. Apparently, the CuTV is part of a PP pattern that forces surrounding air into the low-pressure region below the cloud top. These results further support the well-accepted lateral mixing theory (Heus et al., 2008), but still maintain a possibility that the CuTV can explain observed cloud-top entrainment and bridge the gap between the two theories of lateral versus cloud-top mixing (see Figure A1). The cloud-top mixing theory suggests that most of the environmental air is entrained at the cloud's top, followed by penetrative downdrafts (Paluch, 1979; Squires, 1958).

The humid subsiding shell drew the attention of many studies as it is suspected to isolate the cloud from its environment. Here, we suggest that the downdrafts at the cloud edges are driven by two different processes: (a) a subsiding shell driven by evaporative cooling and negative buoyancy on the cloud edges and (b) CuTV downdrafts resulting from the vorticity field. While the downdrafts of the CuTV appear at the cloud top during its growth stage, the subsiding shell appears during its dissipating stage and in the wake of the ascending cloud top during the growth stage. Since many of the in situ airplane measurements are obtained near cloud tops, it is reasonable to assume that the measured downdrafts (Katzwinkel et al., 2014) contributed to the subsiding shell are actually a combined effect of the latter with the CuTV flow (note that 1D in situ measurements cannot resolve the full 3D structure of the vortex). Nevertheless, the Lagrangian tracers showed that the effect of the CuTV on the

entrained air is similar to the effect of the subsiding humid shell. Despite the relative drying of the descending air (compared to the far environment) shown in Figures 3d and 3f, the air eventually becomes humid (with $RH \approx 94\%$ for cloudy tracers) as it flows through the humid shell before it enters the cloud. The environmental air comprising 90% of the entrained tracers in those layers contains $RH \approx 90\%$ (more humid than the far atmosphere in the cloudy layer). Note that the homogeneous and inhomogeneous mixing models commonly used to study the effects of mixing on the droplet size distribution are hardly distinguishable in such high RH conditions, as the signal of the different processes relies on evaporation. The effects of the CuTV on RH and results of earlier studies (Eytan et al., 2021; Pinsky et al., 2023) suggest that the interaction between the CuTV and the microphysical processes should be further studied. As an example, the 4% of the Lagrangian tracers that were recycled by the vortex can be a source of processed aerosols with the potential of becoming rain embryos.

5.4. Implications for Cumulus Parameterizations

The parametrizations of convection and clouds in most weather and climate models today are based on a steady-state and horizontal homogeneous entraining plume. Climate models show high sensitivity to these parameterizations (Klocke et al., 2011; Romps, 2016; Rougier et al., 2009; Tsushima et al., 2020), leading to high uncertainty in climate prediction (Forster et al., 2021; Sherwood et al., 2014; Zelinka et al., 2020). Several studies over the recent years revealed the important role of transient thermals in atmospheric convection (Hernandez-Deckers et al., 2022; Moser & Lasher-Trapp, 2017; Romps & Charn, 2015; Sherwood et al., 2013; Zhao & Austin, 2005b) and some have already made attempts to construct the corresponding parametrizations (Levine, 1959; Morrison et al., 2020; Pinsky et al., 2023; Yano, 2023). An important part of thermals is their accompanied TV studied here.

The results of this study show that the CuTV plays a dominant role in the mixing of a growing Cu with its environment. These results are encouraging since the CuTV is more deterministic and coherent than the stochastic turbulent motions assumed to govern the mixing process today. Hence, thermals and their accompanied CuTV have the potential to serve as a basis for simplified models (parametrizations) of convective clouds and their mixing processes. Most studies of thermals and CuTVs are based on theory and models. Thus, more effort needs to be focused on observational studies, including both expansions of used techniques (Damiani et al., 2006; Wang & Geerts, 2015), and the development of new methods.

Since climate research and prediction seem to be hampered by large uncertainties stemming from cloud parametrizations, it is important that while the community is working on fixing and improving the current parametrizations, new directions, and theories will be examined. Physics-based novel approaches will improve our understanding of clouds and their role in weather and climate. Hence, they can be used for improving physics-based parametrizations or be incorporated into new data-driven methods, all for advancing weather and climate predictions.

Appendix A: A Simple Model to Estiamte the Scales of the CuTv in Time and Space

The Lagrangian analysis performed here to check what portion of the particles was recycled by the CuTV, used certain thresholds. The equations below estimate the CuTV's motion scales in time and space to support the argument of the expected small Δz for particles recycled by the vortex (see Figure A1 below.) and to justify the threshold chosen to screen out turbulent motions. Assuming a particle trajectory outside the cloud begins at the top of the vortex and ends with its entrainment back into the cloud at the bottom of the vortex. Taking w_{TV} as the vertical velocity of the ascending TV and its entrainment layer, w_{Lp} as the velocity of the Lagrangian particle detrained from the cloud (note that it's negative as the particle is descending), and l_{TV} as the diameter of the vortex, we obtain the following:

$$l_{TV} = \Delta z_{TV} - \Delta z_{Lp} = \Delta t(w_{TV} - w_{Lp}) \tag{A1}$$

$$\Delta t = \frac{l_{TV}}{(w_{TV} - w_{Lp})} \tag{A2}$$

$$\Delta z_{Lp} = w_{Lp}\Delta t = w_{Lp}\frac{l_{TV}}{(w_{TV} - w_{Lp})} \tag{A3}$$

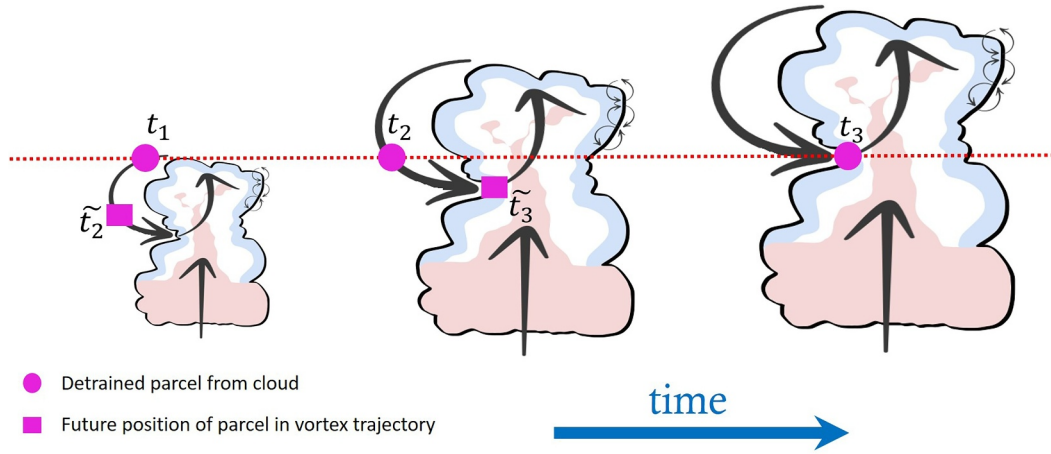

Figure A1. *Schematic of the cloud and CuTV evolution*. The schematic visualizes the expected small Δz, as found by Equation A3. As the cloud grows from left to right, the parcel moves along the trajectory determined by the CuTV. The Magenta dot represents the location of the parcel in each time step. The magenta square represents the position on the vortex's trajectory in the next time step (denoted as $\tilde{t_n}$), considering only the velocity of the parcel relative to the cloud top. The difference between $\tilde{t_n}$ and t_n is caused by the movement of the ascending vortex and the difference between t_n and t_{n+1} is caused by the absolute velocity. The red dashed line is the location of the parcel that stays constant in time when the cloud's top velocity is equal to the downdraft in the CuTV.

Taking w_{Lp} to zero will give a lower bound on Δz_{Lp} with no vertical displacement of the detrained particle. A stationary vortex with $w_{TV} = 0$ gives an upper bound for Δz_{Lp} as we obtain that the displacement is equal to the length of the vortex. In our analysis, we cleared all trajectories with smaller lengths and time scales than the scale of the vortex in order to avoid particles caught in the small-scale turbulent regime near the cloud edge, hence going in and out of the cloud. Assuming $w_{TV} \approx 3\,\frac{m}{s}$, $w_{Lp} \approx -1\,\frac{m}{s}$ and $l_{TV} \approx 400$ m (see Figures 3a and 5a for the chosen scales), yielded a $\Delta z_{Lp} \approx -100$ m and a $\Delta t \approx = 1\frac{2}{3}$ min. Therefore, we chose to limit our analysis to trajectories with $\Delta t \geq 1.5$ min. The normalized distributions of Δz and RH have not changed significantly when choosing the thresholds of $\Delta t \geq 1$ min.

Conflict of Interest

The authors declare no conflicts of interest relevant to this study.

Data Availability Statement

The SAM codes are publicly available at Khairoutdinov (2023). The BOMEX thermodynamic profiles used to initialize the simulation are from Siebesma et al. (2003), while the profiles for the Hawaiian cloud from Supporting Information S1 are publicly available at Oolman (2023). The data used for producing the figures is publicly available as Matlab files at Eytan et al. (2023).

E.E., I.K., and A.K. jointly conceived the principal idea. E.E. carried out the analysis. Y.A. contributed to the Lagrangian analysis. E.E., I.K., A.K., O.A., Y.A., E.G., and M.P. discussed the results and wrote the paper.

Acknowledgments
This paper is one of the last publications of Dr. Mark Pinsky who passed away during the revision process. We were honored to have worked with Mark, a great scientist who made important contributions to cloud physics, all in his characteristically humble way. This project has received funding from the European Research Council (ERC) under the European Union's Horizon 2020 research and innovation programme (CloudCT, Grant 810370), and is supported by the Israel Science Foundation (Grant 1449/22). A. Khain, M. Pinsky, and E. Gavze were supported by the Israel Science Foundation (Grants 2635/20), and partially supported by the Department of Energy (Grant DE-SC008811). E. Eytan was supported by the Institute for Environmental Sustainability (IES) at the Weizmann Institute of Science. Last, we would like to thank the editor and three anonymous reviewers who helped improve the paper.

References

Allan, R. P. (2011). Combining satellite data and models to estimate cloud radiative effect at the surface and in the atmosphere. *Meteorological Applications*, *18*(3), 324–333. https://doi.org/10.1002/met.285

Arakawa, A., & Schubert, W. H. (1974). Interaction of a cumulus cloud ensemble with the large-scale environment, Part i. *Journal of the Atmospheric Sciences*, *31*(3), 674–701. https://doi.org/10.1175/1520-0469(1974)031<0674:ioacce>2.0.co;2

Arieli, Y., Eytan, E., Altaratz, O., Khain, A., & Koren, I. (2024). Distinct mixing regimes in shallow cumulus clouds. *Geophysical Research Letters*, *51*(2), e2023GL105746. https://doi.org/10.1029/2023gl105746

Baker, M., Corbin, R., & Latham, J. (1980). The influence of entrainment on the evolution of cloud droplet spectra: I. A model of inhomogeneous mixing. *Quarterly Journal of the Royal Meteorological Society*, *106*(449), 581–598. https://doi.org/10.1002/qj.49710644914

Carpenter, R. L., Droegemeier, K. K., & Blyth, A. M. (1998). Entrainment and detrainment in numerically simulated cumulus congestus clouds. Part iii: Parcel analysis. *Journal of the Atmospheric Sciences*, *55*(23), 3440–3455. https://doi.org/10.1175/1520-0469(1998)055<3440:eadins>2.0.co;2

Champouillon, A., Rio, C., & Couvreux, F. (2023). Simulating the transition from shallow to deep convection across scales: The role of congestus clouds. *Journal of the Atmospheric Sciences*, *80*(12), 2989–3005. https://doi.org/10.1175/jas-d-23-0027.1

Dabiri, J. O., & Gharib, M. (2004). Fluid entrainment by isolated vortex rings. *Journal of Fluid Mechanics*, *511*, 311–331. https://doi.org/10.1017/s0022112004009784

Damiani, R., Vali, G., & Haimov, S. (2006). The structure of thermals in cumulus from airborne dual-doppler radar observations. *Journal of the Atmospheric Sciences*, *63*(5), 1432–1450. https://doi.org/10.1175/jas3701.1

Dawe, J. T., & Austin, P. H. (2011). Interpolation of les cloud surfaces for use in direct calculations of entrainment and detrainment. *Monthly Weather Review*, *139*(2), 444–456. https://doi.org/10.1175/2010mwr3473.1

De Rooy, W. C., Bechtold, P., Fröhlich, K., Hohenegger, C., Jonker, H., Mironov, D., et al. (2013). Entrainment and detrainment in cumulus convection: An overview. *Quarterly Journal of the Royal Meteorological Society*, *139*(670), 1–19. https://doi.org/10.1002/qj.1959

Eytan, E., Arieli, Y., Khain, A., Altaratz, O., Pinsky, M., Ehud, G., & Koren, I. (2023). Data from: The role of the toroidal vortex in cumulus clouds' entrainment and mixing. https://doi.org/10.34933/wis.000656

Eytan, E., Khain, A., Pinsky, M., Altaratz, O., Shpund, J., & Koren, I. (2022). Shallow cumulus properties as captured by adiabatic fraction in high-resolution LES simulations. *Journal of the Atmospheric Sciences*, *79*(2), 409–428. https://doi.org/10.1175/jas-d-21-0201.1

Eytan, E., Koren, I., Altaratz, O., Pinsky, M., & Khain, A. (2021). Revisiting adiabatic fraction estimations in cumulus clouds: High-resolution simulations with a passive tracer. *Atmospheric Chemistry and Physics*, *21*(21), 16203–16217. https://doi.org/10.5194/acp-21-16203-2021

Fan, J., Ovtchinnikov, M., Comstock, J. M., McFarlane, S. A., & Khain, A. (2009). Ice formation in arctic mixed-phase clouds: Insights from a 3-D cloud-resolving model with size-resolved aerosol and cloud microphysics. *Journal of Geophysical Research*, *114*(D4), D04205. https://doi.org/10.1029/2008jd010782

Forster, P., Storelvmo, T., Armour, K., Collins, W., Dufresne, J.-L., Frame, D., et al. (2021). The earth's energy budget, climate feedbacks, and climate sensitivity 2021. In *The physical science basis. contribution of working group i to the sixth assessment report of the intergovernmental panel on climate change ed v masson-delmotte et al.*

French, J. R., Vali, G., & Kelly, R. D. (1999). Evolution of small cumulus clouds in Florida: Observations of pulsating growth. *Atmospheric Research*, *52*(1–2), 143–165. https://doi.org/10.1016/s0169-8095(99)00024-1

Gerber, H. (2000). Structure of small cumulus clouds. In *Proc. 13th int. conf. on clouds and precipitation* (pp. 105–108).

Gerber, H., Frick, G. M., Jensen, J. B., & Hudson, J. G. (2008). Entrainment, mixing, and microphysics in trade-wind cumulus. *Journal of the Meteorological Society of Japan. Ser. II*, *86*, 87–106. https://doi.org/10.2151/jmsj.86a.87

Gharib, M., Rambod, E., & Shariff, K. (1998). A universal time scale for vortex ring formation. *Journal of Fluid Mechanics*, *360*, 121–140. https://doi.org/10.1017/s0022112097008410

Heiblum, R. H., Pinto, L., Altaratz, O., Dagan, G., & Koren, I. (2019). Core and margin in warm convective clouds–part 1: Core types and evolution during a cloud's lifetime. *Atmospheric Chemistry and Physics*, *19*(16), 10717–10738. https://doi.org/10.5194/acp-19-10717-2019

Hernandez-Deckers, D., Matsui, T., & Fridlind, A. M. (2022). Updraft dynamics and microphysics: On the added value of the cumulus thermal reference frame in simulations of aerosol–deep convection interactions. *Atmospheric Chemistry and Physics*, *22*(2), 711–724. https://doi.org/10.5194/acp-22-711-2022

Heus, T., & Jonker, H. J. (2008). Subsiding shells around shallow cumulus clouds. *Journal of the Atmospheric Sciences*, *65*(3), 1003–1018. https://doi.org/10.1175/2007jas2322.1

Heus, T., Jonker, H. J., Van den Akker, H. E., Griffith, E. J., Koutek, M., & Post, F. H. (2009). A statistical approach to the life cycle analysis of cumulus clouds selected in a virtual reality environment. *Journal of Geophysical Research*, *114*(D6), D06208. https://doi.org/10.1029/2008jd010917

Heus, T., & Seifert, A. (2013). Automated tracking of shallow cumulus clouds in large domain, long duration large eddy simulations. *Geoscientific Model Development*, *6*(4), 1261–1273. https://doi.org/10.5194/gmd-6-1261-2013

Heus, T., Van Dijk, G., Jonker, H. J., & Van den Akker, H. E. (2008). Mixing in shallow cumulus clouds studied by Lagrangian particle tracking. *Journal of the Atmospheric Sciences*, *65*(8), 2581–2597. https://doi.org/10.1175/2008jas2572.1

Hill, M. J. M. (1894). Vi. on a spherical vortex. *Philosophical Transactions of the Royal Society of London*, (185), 213–245.

Kain, J. S., & Fritsch, J. M. (1990). A one-dimensional entraining/detraining plume model and its application in convective parameterization. *Journal of the Atmospheric Sciences*, *47*(23), 2784–2802. https://doi.org/10.1175/1520-0469(1990)047<2784:aodepm>2.0.co;2

Katzwinkel, J., Siebert, H., Heus, T., & Shaw, R. A. (2014). Measurements of turbulent mixing and subsiding shells in trade wind cumuli. *Journal of the Atmospheric Sciences*, *71*(8), 2810–2822. https://doi.org/10.1175/jas-d-13-0222.1

Khain, A., & Pinsky, M. (2018). *Physical processes in clouds and cloud modeling*. Cambridge University Press.

Khain, A., Pokrovsky, A., Pinsky, M., Seifert, A., & Phillips, V. (2004). Simulation of effects of atmospheric aerosols on deep turbulent convective clouds using a spectral microphysics mixed-phase cumulus cloud model. Part i: Model description and possible applications. *Journal of the Atmospheric Sciences*, *61*(24), 2963–2982. https://doi.org/10.1175/jas-3350.1

Khairoutdinov, M. (2023). Sam model code [Software]. Retrieved from http://rossby.msrc.sunysb.edu/SAM.html

Khairoutdinov, M., & Kogan, Y. L. (1999). A large eddy simulation model with explicit microphysics: Validation against aircraft observations of a stratocumulus-topped boundary layer. *Journal of the Atmospheric Sciences*, *56*(13), 2115–2131. https://doi.org/10.1175/1520-0469(1999)056<2115:alesmw>2.0.co;2

Khairoutdinov, M., & Randall, D. (2003). Cloud resolving modeling of the ARM summer 1997 IOP: Model formulation, results, uncertainties, and sensitivities. *Journal of the Atmospheric Sciences*, *60*(4), 607–625. https://doi.org/10.1175/1520-0469(2003)060<0607:crmota>2.0.co;2

Klocke, D., Pincus, R., & Quaas, J. (2011). On constraining estimates of climate sensitivity with present-day observations through model weighting. *Journal of Climate*, *24*(23), 6092–6099. https://doi.org/10.1175/2011jcli4193.1

Konwar, M., Prabhakaran, T., Khain, A., & Pinsky, M. (2021). Cloud microphysical structure analysis based on high-resolution in situ measurements. *Journal of the Atmospheric Sciences*, *78*(7), 2265–2285. https://doi.org/10.1175/jas-d-20-0229.1

Lai, A. C., Zhao, B., Law, A. W.-K., & Adams, E. E. (2015). A numerical and analytical study of the effect of aspect ratio on the behavior of a round thermal. *Environmental Fluid Mechanics*, *15*(1), 85–108. https://doi.org/10.1007/s10652-014-9362-3

Laird, N. F. (2005). Humidity halos surrounding small cumulus clouds in a tropical environment. *Journal of the Atmospheric Sciences*, *62*(9), 3420–3425. https://doi.org/10.1175/jas3538.1

Lecoanet, D., & Jeevanjee, N. (2019). Entrainment in resolved, dry thermals. *Journal of the Atmospheric Sciences*, *76*(12), 3785–3801. https://doi.org/10.1175/jas-d-18-0320.1

Lehmann, K., Siebert, H., & Shaw, R. A. (2009). Homogeneous and inhomogeneous mixing in cumulus clouds: Dependence on local turbulence structure. *Journal of the Atmospheric Sciences*, *66*(12), 3641–3659. https://doi.org/10.1175/2009jas3012.1

Levine, J. (1959). Spherical vortex theory of bubble-like motion in cumulus clouds. *Journal of the Atmospheric Sciences*, *16*(6), 653–662. https://doi.org/10.1175/1520-0469(1959)016<0653:svtobl>2.0.co;2

Lim, J.-S., & Hoffmann, F. (2023). Between broadening and narrowing: How mixing affects the width of the droplet size distribution. *Journal of Geophysical Research: Atmospheres*, *128*(8), e2022JD037900. https://doi.org/10.1029/2022jd037900

McKim, B., Jeevanjee, N., & Lecoanet, D. (2020). Buoyancy-driven entrainment in dry thermals. *Quarterly Journal of the Royal Meteorological Society*, *146*(726), 415–425. https://doi.org/10.1002/qj.3683

Meleshko, V., Gourjii, A., & Krasnopolskaya, T. (2012). Vortex rings: History and state of the art. *Journal of Mathematical Sciences*, *187*(6), 772–808. https://doi.org/10.1007/s10958-012-1100-0

Morrison, H., Jeevanjee, N., Lecoanet, D., & Peters, J. M. (2023). What controls the entrainment rate of dry buoyant thermals with varying initial aspect ratio? *Journal of the Atmospheric Sciences*, *80*(11), 2711–2728. https://doi.org/10.1175/jas-d-23-0063.1

Morrison, H., Jeevanjee, N., & Yano, J.-I. (2022). Dynamic pressure drag on rising buoyant thermals in a neutrally stable environment. *Journal of the Atmospheric Sciences*, *79*(11), 3045–3063. https://doi.org/10.1175/jas-d-21-0274.1

Morrison, H., Peters, J. M., & Sherwood, S. C. (2021). Comparing growth rates of simulated moist and dry convective thermals. *Journal of the Atmospheric Sciences*, *78*(3), 797–816. https://doi.org/10.1175/jas-d-20-0166.1

Morrison, H., Peters, J. M., Varble, A. C., Hannah, W. M., & Giangrande, S. E. (2020). Thermal chains and entrainment in cumulus updrafts. Part i: Theoretical description. *Journal of the Atmospheric Sciences*, *77*(11), 3637–3660. https://doi.org/10.1175/jas-d-19-0243.1

Moser, D. H., & Lasher-Trapp, S. (2017). The influence of successive thermals on entrainment and dilution in a simulated cumulus congestus. *Journal of the Atmospheric Sciences*, *74*(2), 375–392. https://doi.org/10.1175/jas-d-16-0144.1

Oolman, L. (2023). Radiosonde profiles [Dataset]. *University of Wyoming, Atmospheric Science Department*. Retrieved from https://weather.uwyo.edu/upperair/sounding.html

Paluch, I. R. (1979). The entrainment mechanism in Colorado cumuli. *Journal of the Atmospheric Sciences*, *36*(12), 2467–2478. https://doi.org/10.1175/1520-0469(1979)036<2467:temicc>2.0.co;2

Perry, K. D., & Hobbs, P. V. (1996). Influences of isolated cumulus clouds on the humidity of their surroundings. *Journal of the Atmospheric Sciences*, *53*(1), 159–174. https://doi.org/10.1175/1520-0469(1996)053<0159:ioicco>2.0.co;2

Pinsky, M., Eytan, E., Gavze, E., & Khain, A. (2023). Vortex structure of head bubble in convective cloud starting plume. *Journal of the Atmospheric Sciences*, *80*(8), 2091–2113. https://doi.org/10.1175/jas-d-22-0122.1

Pinsky, M., Eytan, E., Koren, I., Altaratz, O., & Khain, A. (2021). Convective and turbulent motions in non-precipitating cu. Part 1: Method of separation of convective and turbulent motions. *Journal of the Atmospheric Sciences*, *78*(7), 2307–2321. https://doi.org/10.1175/jas-d-20-0127.1

Pinsky, M., Eytan, E., Koren, I., & Khain, A. (2022). Convective and turbulent motions in nonprecipitating cu. Part ii: Les simulated cloud represented by a starting plume. *Journal of the Atmospheric Sciences*, *79*(3), 793–813. https://doi.org/10.1175/jas-d-21-0137.1

Pinsky, M., & Khain, A. (2018). Theoretical analysis of the entrainment–mixing process at cloud boundaries. Part i: Droplet size distributions and humidity within the interface zone. *Journal of the Atmospheric Sciences*, *75*(6), 2049–2064. https://doi.org/10.1175/jas-d-17-0308.1

Pinsky, M., & Khain, A. (2023). Convective and turbulent motions in nonprecipitating cu. Part iii: Characteristics of turbulence motions. *Journal of the Atmospheric Sciences*, *80*(2), 457–471. https://doi.org/10.1175/jas-d-21-0223.1

Rio, C., Del Genio, A. D., & Hourdin, F. (2019). Ongoing breakthroughs in convective parameterization. *Current Climate Change Reports*, *5*(2), 95–111. https://doi.org/10.1007/s40641-019-00127-w

Romps, D. M. (2010). A direct measure of entrainment. *Journal of the Atmospheric Sciences*, *67*(6), 1908–1927. https://doi.org/10.1175/2010jas3371.1

Romps, D. M. (2016). The stochastic parcel model: A deterministic parameterization of stochastically entraining convection. *Journal of Advances in Modeling Earth Systems*, *8*(1), 319–344. https://doi.org/10.1002/2015ms000537

Romps, D. M., & Charn, A. B. (2015). Sticky thermals: Evidence for a dominant balance between buoyancy and drag in cloud updrafts. *Journal of the Atmospheric Sciences*, *72*(8), 2890–2901. https://doi.org/10.1175/jas-d-15-0042.1

Romps, D. M., Öktem, R., Endo, S., & Vogelmann, A. M. (2021). On the life cycle of a shallow cumulus cloud: Is it a bubble or plume, active or forced? *Journal of the Atmospheric Sciences*, *78*(9), 2823–2833. https://doi.org/10.1175/jas-d-20-0361.1

Rougier, J., Sexton, D. M., Murphy, J. M., & Stainforth, D. (2009). Analyzing the climate sensitivity of the HadSM3 climate model using ensembles from different but related experiments. *Journal of Climate*, *22*(13), 3540–3557. https://doi.org/10.1175/2008jcli2533.1

Sau, R., & Mahesh, K. (2007). Passive scalar mixing in vortex rings. *Journal of Fluid Mechanics*, *582*, 449–461. https://doi.org/10.1017/s0022112007006349

Savarin, A., & Chen, S. S. (2022). Pathways to better prediction of the MJO–part i: Effects of model resolution and moist physics on atmospheric boundary layer and precipitation. *Journal of Advances in Modeling Earth Systems*, *14*(6), e2021MS002928. https://doi.org/10.1029/2021ms002928

Sherwood, S. C., Bony, S., & Dufresne, J.-L. (2014). Spread in model climate sensitivity traced to atmospheric convective mixing. *Nature*, *505*(7481), 37–42. https://doi.org/10.1038/nature12829

Sherwood, S. C., Hernández-Deckers, D., Colin, M., & Robinson, F. (2013). Slippery thermals and the cumulus entrainment paradox. *Journal of the Atmospheric Sciences*, *70*(8), 2426–2442. https://doi.org/10.1175/jas-d-12-0220.1

Siebesma, A. P., Bretherton, C. S., Brown, A., Chlond, A., Cuxart, J., Duynkerke, P. G., et al. (2003). A large eddy simulation intercomparison study of shallow cumulus convection. *Journal of the Atmospheric Sciences*, *60*(10), 1201–1219. https://doi.org/10.1175/1520-0469(2003)60%3C1201:ALESIS%3E2.0.CO;2

Squires, P. (1958). The microstructure and colloidal stability of warm clouds. *Tellus*, *10*(2), 262–271. https://doi.org/10.1111/j.2153-3490.1958.tb02012.x

Strauss, C., Ricard, D., & Lac, C. (2022). Dynamics of the cloud–environment interface and turbulence effects in an LES of a growing cumulus congestus. *Journal of the Atmospheric Sciences*, *79*(3), 593–619. https://doi.org/10.1175/jas-d-20-0386.1

Süli, E., & Mayers, D. F. (2003). *An introduction to numerical analysis*. Cambridge University Press.

Tiedtke, M. (1989). A comprehensive mass flux scheme for cumulus parameterization in large-scale models. *Monthly Weather Review*, *117*(8), 1779–1800. https://doi.org/10.1175/1520-0493(1989)117<1779:acmfsf>2.0.co;2

Trenberth, K. E., Fasullo, J. T., & Kiehl, J. (2009). Earth's global energy budget. *Bulletin of the American Meteorological Society*, *90*(3), 311–323. https://doi.org/10.1175/{2008BAMS2634}.1

Tsushima, Y., Ringer, M. A., Martin, G. M., Rostron, J. W., & Sexton, D. M. (2020). Investigating physical constraints on climate feedbacks using a perturbed parameter ensemble. *Climate Dynamics*, *55*(5), 1159–1185. https://doi.org/10.1007/s00382-020-05318-y

Turner, J. (1962). The 'starting plume'in neutral surroundings. *Journal of Fluid Mechanics*, *13*(3), 356–368. https://doi.org/10.1017/s0022112062000762

Villalba-Pradas, A., & Tapiador, F. J. (2022). Empirical values and assumptions in the convection schemes of numerical models. *Geoscientific Model Development*, *15*(9), 3447–3518. https://doi.org/10.5194/gmd-15-3447-2022

Vybhav, G., & Ravichandran, S. (2022). Entrainment in dry and moist thermals. *Physical Review Fluids*, *7*(5), 050501. https://doi.org/10.1103/physrevfluids.7.050501

Wang, Y., & Geerts, B. (2015). Vertical-plane dual-Doppler radar observations of cumulus toroidal circulations. *Journal of Applied Meteorology and Climatology*, *54*(10), 2009–2026. https://doi.org/10.1175/jamc-d-14-0252.1

Yano, J.-I. (2014). Basic convective element: Bubble or plume? A historical review. *Atmospheric Chemistry and Physics*, *14*(13), 7019–7030. https://doi.org/10.5194/acp-14-7019-2014

Yano, J.-I. (2023). Similarity solutions of thermal vortex rings: Vorticity-dynamics-based derivation. *AIP Advances*, *13*(4), 045123. https://doi.org/10.1063/5.0129309

Zelinka, M. D., Myers, T. A., McCoy, D. T., Po-Chedley, S., Caldwell, P. M., Ceppi, P., et al. (2020). Causes of higher climate sensitivity in CMIP6 models. *Geophysical Research Letters*, *47*(1), e2019GL085782. https://doi.org/10.1029/2019gl085782

Zhao, M., & Austin, P. H. (2005a). Life cycle of numerically simulated shallow cumulus clouds. Part i: Transport. *Journal of the Atmospheric Sciences*, *62*(5), 1269–1290. https://doi.org/10.1175/jas3414.1

Zhao, M., & Austin, P. H. (2005b). Life cycle of numerically simulated shallow cumulus clouds. Part ii: Mixing dynamics. *Journal of the Atmospheric Sciences*, *62*(5), 1291–1310. https://doi.org/10.1175/jas3415.1